Numerical simulations of inhomogeneous superconducting films

A study of anisotropy and dendritic flux avalanches in samples with line pattern of reduced critical current

Knut Tyse

Master Thesis

For the degree of Master of Science in condensed matter physics

The Faculty of Mathematics and Natural Sciences

University of Oslo

04/07/2016

Numerical simulations of inhomogeneous superconducting films

http://www.duo.uio.no/

Print: Reprosentralen, Universitetet i Oslo

"The noblest pleasure is the joy of understanding."

Leonardo da Vinci

Abstract

We have done computer simulations on the electrodynamics of rectangular superconducting films. The critical sheet current is an isotropic quantity. By reducing the critical sheet current in a stripe pattern, we have produced approximately 10 % anisotropy in the macroscopic current. We have also studied the two-dimensional branching patterns that are produced by magnetic flux avalanches in our perturbed samples. While the traditional dendritic patterns constitute the core of the avalanche, we also see branches that are aligned with the borders between high and low critical sheet current. The latter branching pattern has been investigated in great detail in order to increase our understanding of magnetic flux avalanches in superconducting films. We have also developed a computer algorithm for drawing Bean model streamlines. While it was intended for studying the supercurrent in our perturbed samples, it should also be a valuable tool for studies of the Bean model in various geometries.

Acknowledgements

In my work I have used Jørn Inge Vestgården's program for simulating electrodynamics in superconducting films. I want to thank him for letting me use this sophisticated piece of software and help me understand the implementation. He also is one of the most thorough scientists I know and I have adapted his habits for systematic scientific study. Pavlo Mikheenko has a long and diverse experience to draw from, both in theory and application. He has enormous ambitions for his field of research and shared his knowledge with great enthusiasm. I have worked closely with Thomas Håbu Qureishy. His theoretical knowledge of material science and practical skills in analysis of materials were appreciated in our group. The theoretical studies in this thesis are inspired by the experimental work of T. Qureishy and P. Mikheenko. I have had fruitful discussions with Professor Tom Henning Johansen, whenever my research touched on his fields of expertise.

In my work I have benefited greatly from scientific software. Matplotlib has produced beautiful and informative plots. The Julia programming language combines a simple syntax, a large standard library and fast computation. I want to thank the developers of LaTeX for the formatting of this thesis. Tikz has let me draw professional looking figures to include in my LaTeX files. The thesis was compiled by overleaf.com, letting me spend more of my time on research and writing.

Contents

Physical Constants

Speed of Light	c	$=$	$2.997\ 924\ 58 \times 10^{8}\,\mathrm{m\ s^{-1}}$
Electron mass	m	$=$	$9.109\ 383\ 56 \times 10^{-31}\,\mathrm{kg}$
Electron charge	e	$=$	$-1.602\ 176\ 6208 \times 10^{-19}\,\mathrm{C}$
The permeability of vacuum	μ_0	$=$	$4\pi \times 10^{-7}\,\mathrm{N\,A^{-2}}$
Plank's constant	h	$=$	$6.626\ 070\ 040 \times 10^{-34}\mathrm{m^2\,kg\,s^{-1}}$
The magnetic flux quantum	Φ_0	$=$	$2.067\ 833\ 831 \times 10^{-15}\,\mathrm{Wb}$

To my mother and father who encouraged my curiosity for the universe.

Chapter 1

Introduction

Superconducting films are used in technological applications where it is necessary that the superconductors have high resistance to external magnetic field. It is therefore of great importance to understand the electrodynamic behavior of such films. In some superconductors the current can become much stronger in certain directions along the crystal lattice of the material. We say that the current is anisotropic. Unfortunately we are not able to do computer simulations of such material effects. However we can reduce the local critical current in a periodic stripe pattern which makes the current anisotropic on the macroscopic scale.

Thermo-electrical instabilities are a serious problem in practical applications of superconductors. They occur when the superconducting state breaks down locally and in turn destroys the superconducting state in the neighboring regions. We have investigated breakdown of the superconducting state in the perturbed samples mentioned in the above paragraph. The breakdown results in avalanches of magnetic flux which make new and interesting patterns of flux.

This thesis investigates a method of artificially producing anisotropic current in superconducting films. We will also study the flux patterns produced by magnetic flux avalanches in such films.

1.1 Superconductivity

Superconductors are materials with extraordinary electromagnetic properties. Their electrical resistance drops to zero when the temperature of the material is below the *critical temperature* T_c. When a material becomes superconducting it enters a superconducting phase. If the material becomes nonsuperconducting it enters the *normal phase*.

1.2 Type I superconductors

Superconducting materials are divided into two groups: Type I and type II. Most of the elementary metals are type I superconductors. Examples are mercury, aluminium and lead. Type I superconductors generally have critical temperatures below 10 K [1], p. 2. Many of them have T_c smaller than 1 K. Additionally their critical magnetic fields are low.
A type I material will be superconducting if all the following criteria are met:

- The temperature of the material does not exceed the critical temperature T_c.
- The current density does not exceed the critical current density j_c.
- The applied magnetic field, H_a, does not exceed the critical magnetic field H_c.

The values for T_c, j_c and H_c are specific to materials and specimens.

The *Meissner state* is the name of the superconducting state available to type I superconductors [2]. If placed in a magnetic field, the material will induce a *Meissner current* on the surface. This current produces a magnetic field that is equal in magnitude, yet antiparallel to the external field. Therefore the internal field will be $\mathbf{H}_{internal} = 0$ in the Meissner state. This phenomena makes type I superconductors act like perfect diamagnets. Because there is no electrical resistance the Meissner current will persist without decay. Therefore the magnitude of the magnetization is proportional to the external field, while the direction of the magnetization is antiparallel to the external field. This holds as long as $H_a < H_c$. At $H = H_c$ we have a transition to the normal state. This transition will be discontinuous as a function of the applied field. When the material enters the normal state, the screening currents will decay quickly. Because of this the transition will also be very sharp as a function of time. The critical magnetic field H_c is a function of temperature T [1], p. 2:

$$H_c(T) = H_c(T = 0)[1 - (T/T_c)^2] \tag{1.1}$$

As we cannot study materials at absolute zero temperature, we have to extrapolate our experimental data to $T = 0$ K in order to find the value for $H_c(T = 0)$ for a given specimen. The temperature dependence of H_c is shown as a phase diagram in Figure 1.1. The critical current density j_c decreases when temperature and magnetic field decreases.

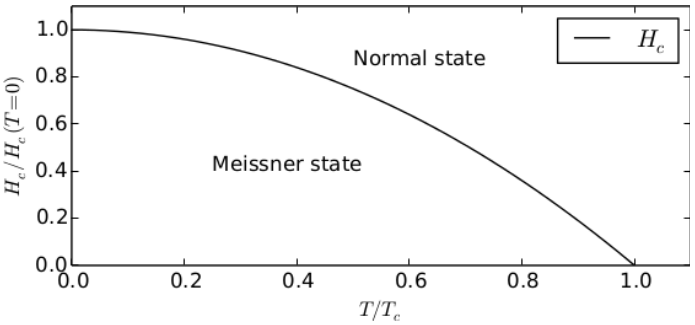

Figure 1.1: Phase diagram for the Meissner state.

1.3 The London theory for superconductors

The London theory [3] was developed by F. London and H. London. The purpose of the theory was to be in agreement with the experiments done by Meissner and Ochenfeld [2]. The London theory established how the electrical field $\mathbf{E}$ and the magnetic field $\mathbf{H}$ are related to the current density $\mathbf{j}$ in the Meissner state:

$$\begin{aligned} \mathbf{E} &= \Lambda \left(\mathbf{j} + c^2 \nabla \rho \right) \\ \mathbf{H} &= -\Lambda c \nabla \times \mathbf{j} \end{aligned} \tag{1.2}$$

Here $\Lambda = m/ne^2$ where m, n and e are the mass, concentration and charge of free electrons. ρ is the charge density and c is the speed of light. Another result of the London theory [3] was that

$$\Lambda c^2 \nabla^2 \mathbf{H} = \mathbf{H} \tag{1.3}$$

in the Meissner state.

Let us consider a superconductor with smooth surfaces. We focus on a small region near the surface of the material and define the local surface field to be $\mathbf{H} = \mathbf{H}_0$. If the surface is large and flat, we can also assume that the magnetic field is parallel to the surface at the surface. We define the x-axis to be normal to the surface, pointing into the material and that $x = 0$ at the surface. From Equation 1.3 we can find the magnetic field profile inside the surface of the material:

$$\Lambda c^2 \frac{\partial^2 \mathbf{H}}{\partial x^2} = \mathbf{H} \tag{1.4}$$

Solving the above differential equation for $x > 0$ we find that

$$\mathbf{H}(x) = \mathbf{H}_0 \exp\left(\pm x / c\sqrt{\Lambda} \right) + \mathbf{C} \tag{1.5}$$

where $\mathbf{C}$ is a constant of integration. According to the Meissner state the internal field of the superconductor shall be zero. Therefore the sign in the exponential function must

be negative and the integration constant must be zero:

$$\mathbf{H}(x) = \mathbf{H}_0 \exp\left(-x/c\sqrt{\Lambda}\right) \tag{1.6}$$

In modern textbooks [1], p. 24, Equation 1.6 if often written as

$$\mathbf{H}(x) = \mathbf{H}_0 \exp\left(-x/\lambda\right), \tag{1.7}$$

where

$$\lambda^2 = \frac{mc^2}{4\pi n_s e^2} \tag{1.8}$$

As before m, n and e are the mass, concentration and charge of free electrons; c is the speed of light. λ is *the London length* of the material, the depth where the field decays to $e^{-1}\mathbf{H_0}$. See Figure 1.2 for an illustration of the solution given by Equation 1.7. Typically λ is about 50 nm for type I materials [1], p. 25. In other words the skin depth of magnetic field is very shallow for type I materials in the Meissner state.

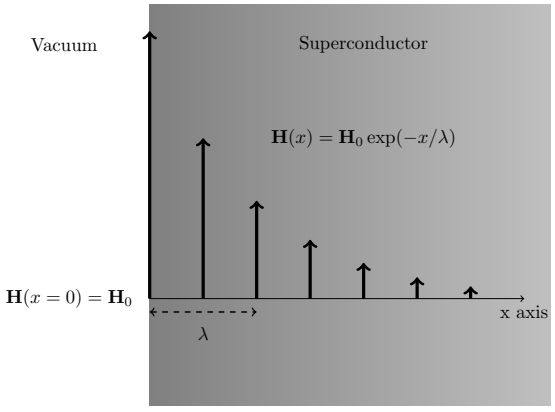

Figure 1.2: The spatial decay of magnetic field from the surface of a bulk superconductor according to the London theory. The gray area represents a small section of the superconductor near the surface of the specimen.

The original paper [3] studies, among other cases, the current and magnetic field of a straight infinite superconducting wire of radius a carrying a current I. Provided that the radius a of the wire is much greater than $0.1\,\mu$m, the radial profile of current and magnetic field was calculated to decay exponentially with depth. Using r as the radial distance from the center of the wire we have:

For $r \leq a$:

$$\begin{aligned} J = J_z &= I\frac{\beta}{2\pi\sqrt{ar}}\exp(\beta(r-a)) \\ H = H_\phi &= I\frac{1}{2\pi c\sqrt{ar}}\exp(\beta(r-a)) \\ \beta^2 &= 1/\Lambda c^2 \end{aligned} \tag{1.9}$$

For $r > a$ (outside the wire):

$$\begin{aligned} J &= 0 \\ H &= H_\phi = I/2\pi rc \end{aligned} \tag{1.10}$$

The magnetic field in Equation 1.10 is simply the magnetic field outside an infinite straight wire carrying a current I.

1.4 Ginzburg - Landau theory

Ginzburg-Landau theory [1], chapter 3, uses an order parameter $\Psi(\mathbf{r})$ to describe the phase transition between the superconducting and the normal state. At the same time $\Psi(\mathbf{r})$ represents the wave function of superconducting electrons. Therefore $\Psi(\mathbf{r})$ is generally considered to be a complex function. The advantage of the Ginzburg-Landau theory is that the effects of quantum mechanics is included by the quantum mechanical properties of Ψ. In a normal material we don't have any superconducting electrons and this implies that $|\Psi(\mathbf{r})|^2 = 0$ in such materials. $|\Psi(\mathbf{r})|^2$ will have a finite value in a superconducting material. Formally we have:

$$\begin{aligned} \Psi &= 0 \quad \text{for} \quad T \geq T_c \\ \Psi &\neq 0 \quad \text{for} \quad T < T_c \end{aligned} \tag{1.11}$$

We see that the order parameter changes continuously around the critical temperature. However, the change between

$$|\Psi|^2 = 0 \text{ and } |\Psi|^2 > 0$$

is discontinuous.

In Landau theory [4] one is interested in the physics close to the phase transition. The simplest case one can study is a superconductor with no external magnetic field and a uniform concentration of superconducting electrons. Near the critical temperature one can do the following expansion of the free energy density:

$$F_{s0} = F_n + \alpha|\Psi|^2 + \frac{\beta}{2}|\Psi|^4 \tag{1.12}$$

F_n is the free energy density of the normal material. The subscript in F_{s0} refers to the superconducting state and zero external field.

In order to find conditions for α and β one has to minimize the free energy in Equation 1.12. When imposing the conditions in Equation 1.11 one finds that $\alpha \propto T - T_c$ and $\beta = constant > 0$. This information can be used for the more general case when the external magnetic field is nonzero and $|\Psi(\mathbf{r})|^2$ is not uniform. In that case we have the more general Gibbs function [1] (using g Gaussian units and with some slight modifications to the nomenclature):

$$G_{sH} = G_n + \alpha|\Psi|^2 + \frac{\beta}{2}|\Psi|^4 + \frac{1}{4m}\left|-ih\nabla\Psi - \frac{2e}{c}\mathbf{A}\right|^2 + \frac{H^2}{8\pi} - \frac{\mathbf{H}\cdot\mathbf{H_0}}{4\pi} \tag{1.13}$$

Here G_n is the Gibbs energy density for the normal state, m is the electron mass, $\mathbf{A}$ is the magnetic vector potential, $\mathbf{H}$ is the local magnetic field and $\mathbf{H}_0$ is the applied magnetic field. The kinetic energy of electrons in a magnetic vector potential $\mathbf{A}$ is included by the term

$$\frac{1}{4m}\left|-ih\nabla\Psi - \frac{2e}{c}\mathbf{A}\right|^2 \tag{1.14}$$

The magnetic energy density is included by the terms

$$\frac{H^2}{8\pi} - \frac{\mathbf{H}\cdot\mathbf{H_0}}{4\pi} \tag{1.15}$$

The total Gibbs energy for the material is found by doing the volume integral of Equation 1.13. By minimizing the result one can find conditions for the functions $|\Psi(\mathbf{r})|^2$ and $\mathbf{A}(\mathbf{r})$:

$$\alpha\Psi + \beta\Psi|\Psi|^2 + \frac{1}{4m}\left(i\hbar\nabla + \frac{2e}{c}\mathbf{A}\right) = 0 \tag{1.16}$$

and

$$\mathbf{j_s} = \frac{c}{4\pi}\nabla\times\nabla\times\mathbf{A} = -\frac{i\hbar e}{2m}(\Psi^*\nabla\Psi - \Psi\nabla\Psi^2) - \frac{2e^2}{mc}|\Psi|^2\mathbf{A} \tag{1.17}$$

It is possible to write Equation 1.16 and Equation 1.17 on a simpler form by defining the following quantities [1], p. 50:

$$\psi(\mathbf{r}) = \Psi(\mathbf{r})/\Psi_0 \quad , \quad \Psi_0^2 = n_s/2 = |\alpha|/\beta, \tag{1.18}$$

where

$$\xi^2 = \frac{\hbar^2}{4m|\alpha|} \quad , \quad \lambda^2 = \frac{mc^2}{4\pi n_s e^2|\alpha|} = \frac{mc^2\beta}{8\pi e^2|\alpha|}.$$

The order parameter is assumed to reach its maximum value deep inside the superconductor. ψ is normalized to this maximum value so that $\psi = 1$ deep inside the superconductor. As in Section 1.3, λ is the London magnetic field penetration depth. ξ is the characteristic length scale for variation in the order parameter and is called the *coherence length*. Therefore ξ characterizes the decay rate of the order parameter near the interface between a superconductor and a normal metal. superconducting material.

The ratio between λ and ξ is called the *Ginzburg - Landau parameter*:

$$\kappa = \lambda/\xi \tag{1.19}$$

Consider an interface between a superconductor and a normal material. If one does integrates the Gibbs energy density across the interface [1], p.p. 57-62, one finds that the energy at the interface depends on λ and ξ. Calculations show that $\kappa < 1/\sqrt{2}$ yields a positive energy at the interface. It is common to refer to this as positive surface tension as the field experiences an outward pressure when trying to enter the superconductor. On the other hand, when $\kappa > 1/\sqrt{2}$, the surface tension is said to be negative. This means that when $\kappa > 1/\sqrt{2}$ the energy of the system decreases when magnetic field enters the material. The Ginzburg-Landau theory predicts two types of superconductors:

- Type I: $\kappa < 1/\sqrt{2}$
- Type II: $\kappa > 1/\sqrt{2}$

1.5 Type II superconductors

For type II superconductors there are two critical fields [1], p. 12. They are called H_{c1} and H_{c2}, with $H_{c1} \ll H_{c2}$. A type II superconductor will be in the Meissner state when all the following conditions are true:

- $T \leq T_c$
- $j \leq j_c$
- $H \leq H_{c1}$

When $H > H_{c1}$, a type II material will transition to what is called *the mixed state*. Tiny threads of magnetic flux are allowed to penetrate the superconductor. In the center of the flux threads the material transitions to the normal state. Thus in the mixed state the material is a mixture of superconducting and normal domains, hence the name. The conditions for the mixed state are as follows:

- $T \leq T_c$
- $j \leq j_c$
- $H_{c1} < H < H_{c2}$

Note that the conditions for temperature and current density are the same for the mixed state and the Meissner state. A phase diagram with respect to temperature and magnetic field is shown in Figure 1.3.

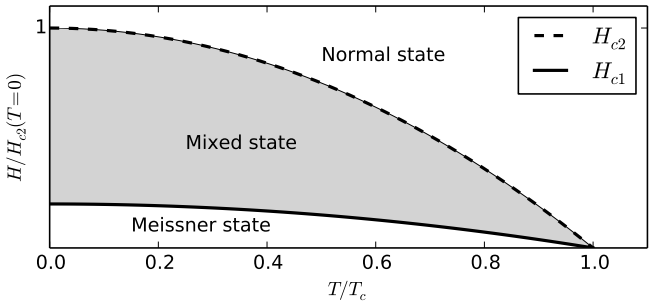

Figure 1.3: The phase diagram for type II superconductors. The figure is not to scale; remember that $H_{c1} \ll H_{c2}$.

In the mixed state, the superconductor will include an increasing number of flux threads as the applied field increases. As these threads are directed in the same direction as the external field, the magnetization of the material will decrease in magnitude until it becomes zero at $H = H_{c2}$[1].

1.5.1 Abrikosov vortices

Alexei Abrikosov's original paper [5] gives a theoretical explanation for the flux thread phenomenon in type II materials. Abrikosov considered a superconductor placed in an external magnetic field **H** parallel to the z-axis. Thus the magnetic vector potential **A** is parallel to the y-axis. Near the transition to the normal state the order parameter is small, $\psi \ll 1$, and Abrikosov assumed the magnetic field to be constant to a first approximation:

$$\mathbf{H} = H_0\hat{\mathbf{z}} \quad \text{and} \quad A_y = H_0 x \tag{1.20}$$

The first Ginzburg-Landau equation is nonlinear in Ψ, but the non-linear term can be ignored near the phase transition because $\psi \ll 1$:

$$\alpha\Psi + \cancel{\beta\Psi|\Psi|^2} + \frac{1}{4m}\left(i\hbar\nabla + \frac{2e}{c}\mathbf{A}\right) = 0 \tag{1.21}$$

By inserting $\mathbf{A} = A_y\hat{j}$ from Equation 1.20 and simplifying the resulting equation, the original paper arrives at the harmonic oscillator equation known from quantum mechanics. The equation has the solution

$$\psi = \sum_{n=-\infty}^{\infty} C_n \exp(ikny) \exp\left(-\frac{\kappa^2}{2}\left(x - kn/\kappa^2\right)^2\right) \tag{1.22}$$

where k is a spatial frequency and κ is the Ginzburg-Landau parameter. ψ is the dimensionalless order parameter defined in Equation 1.18. This solution is inserted in the

[1]The magnetization in the normal state is very small.

second Ginzburg-Landau equation. The paper continues by deriving the conditions for H_0, ψ and C_n. By requiring minimum energy, Abrikosov calculates a solution $\psi(x, y)$ that is periodic along the x and y axis. Moreover ψ is symmetric by 90^o rotation in the xy-plane. ψ has maxima in magnetic field that correspond to minima in the order parameter. The original paper interprets the maxima in magnetic field as where the flux threads penetrate. The material is in the normal state in the center of the flux threads. The flux threads are centered inside a current vortex which screens the superconducting domains from magnetic field. Such currents vortices are now called Abrikosov vortices. Experiments show that the vortices tend to be arranged in a hexagonal lattice [6]. This geometry was suggested in Abrikosov's paper, but yielded a higher energy than the square lattice. Because of experimental validation, the Nobel Prize in Physics was awarded to Alexei A. Abrikosov, Vitaly L. Ginzburg and Anthony J. Leggett in 2003 [7]. The total magnetic flux through a vortex is quantized to

$$\Phi_0 = \frac{h}{2e} \approx 2.07 \cdot 10^{-15} \text{ Wb} \tag{1.23}$$

which is called the a flux-quant [1], p. 29. Here h, c and e are Planck's constant, the speed of light and the electron charge respectively. The field going through the center of a vortex is commonly referred to as flux threads or flux lines. A superconductor is in the mixed state when it is penetrated by flux vortices. For this reason we also call the mixed state for the *vortex state*.

1.6 Electromagnetism in the mixed state

While the Meissner state implies several conditions, like zero internal magnetic and electric fields, the mixed state has more freedom. In this section we will introduce the electromagnetic relations used in the literature, e.g. Brandt [8]. The following relations work well when we are considering phenomena on a length scale much larger that the diameter of the Abrikosov vortices.

Provided that electric field $\mathbf{E}$ is varying slowly, we can ignore the displacement current and use the original version of Ampère's law:

$$\nabla \times \mathbf{H} = \mathbf{j} \tag{1.24}$$

The Maxwell-Faraday equation states that

$$\nabla \times \mathbf{E} = -\dot{\mathbf{B}} \tag{1.25}$$

Here we have used dot notation for the time derivative of the magnetic flux density $\mathbf{B}$. By doing the substitution $\mathbf{B} = \mu_0 \mathbf{H}$, where μ_0 is the permeability constant, we can write

Equation 1.25 in terms of the magnetic field strength **H**:

$$\nabla \times \mathbf{E} = -\mu_0 \dot{\mathbf{H}} \Rightarrow \dot{\mathbf{H}} = -\frac{1}{\mu_0} \nabla \times \mathbf{E} \tag{1.26}$$

From Equation 1.26 we see that the electric field can become nonzero if the magnetic field changes in time. The electric field is parallel with the current density vector:

$$\mathbf{E} = \rho \mathbf{j} \tag{1.27}$$

We have used **j** as the symbol for current density, however **J** is often used in the more general literature on electromagnetism. ρ is the resistivity of the superconducting material provided that $\mathbf{j} \perp \mathbf{B}$. The paradox of electrical resistance in superconductors appears when the electrical field is non-zero. The internal electrical field is zero in the Meissner state, but this is not generally true in the mixed state. By inserting Equation 1.27 into Equation 1.26 we get the following expression for the time derivative of the magnetic field:

$$\dot{\mathbf{H}} = -\frac{\rho}{\mu_0} \nabla \times \mathbf{j} \tag{1.28}$$

Whenever the electrical field is nonzero, there will be dissipation of heat given by

$$p = \mathbf{j} \cdot \mathbf{E} \tag{1.29}$$

The magnetization of a superconductor is calculated by integrating the cross product of **r** and **j** over the volume of the specimen:

$$\mathbf{m} = \frac{1}{2} \int \mathbf{r} \times \mathbf{j} \, d^3 r \tag{1.30}$$

Local fluctuations in the density of electrical charge are possible:

$$q = \epsilon_0 \nabla \cdot \mathbf{E} = \epsilon_0 \rho \nabla \cdot \mathbf{j} \tag{1.31}$$

The screening current in the mixed state produces a Lorentz force $\mathbf{F}_L$ [9] which acts on the flux-threads:

$$\mathbf{F}_L = \mathbf{j} \times \mathbf{\Phi}_0 \tag{1.32}$$

Where $\mathbf{\Phi}_0 = h/2e$ is the flux quantum, which is parallel to the applied field. h is the Planck's constant and e is the electron charge. The Lorentz force pushes the vortices in the direction of lower current density.

1.7 Material properties in the mixed state

The counter force to the Lorentz force is the pinning force. Type II superconductors are designed to have defects in the crystal which do not transition to the superconducting state. It is energetically favorable for flux to go through these normal defects. Such regions of lower potential energy are called pinning potentials or pinning centers. This is because the Lorentz force must do work on the flux line in order to move it out of the pinning potential and into the superconductor. Y. B. Kim et al [10] calculated the decay of persistent currents from experiment and related it to dissipation caused by flux motion. The currents decreased at a rate proportional to $-\ln(t)$ where t is time. The fastest decay rate found in [10] implied that the currents would still survive for a very long time: $3 \cdot 10^{92}$ years.

A theoretical explanation written by P. W. Anderson's followed shortly [11]. The rate R at which flux escapes the pinning potential was found to be proportional to the Boltzman factor corresponding to the energy difference between the superconducting and the normal state. In other words thermal energy can assist flux threads when they escape the pinning potentials. This type of flux motion is called *flux creep* and leads to local fluctuations in temperature. Because flux creep depends on activation energy, we see less flux creep at lower temperatures.

While there are several models for the resistivity ρ for the mixed state, we will be using the power law [8]:

$$E(j) = E_c(j/j_c)^n, \tag{1.33}$$

where

$$E_c = E(j_c)$$

is the critical electric field when $j = j_c$. Equation 1.27 can be inserted into Equation 1.33, which yields

$$\begin{aligned} \rho j &= E_c(j/j_c)^n \\ \rho &= E_c j^{n-1}/j_c^n \end{aligned} \tag{1.34}$$

When $n = 1$ we have ohmic resistance. We see that, for large n, ρ becomes large when $j > j_c$ and vanishes when $j < j_c$. These expressions assume that j_c is not anisotropic. The exponent n in Equation 1.34 is a function of temperature and therefore characterizes the rate of flux creep. A large n (100) corresponds to slow flux creep and a small value for n (10) to a faster rate of creep.

1.8 The Bean model

Before the theory of flux threads in the mixed state had been proven by experiments, Charles Bean constructed a model for penetration of current and magnetic field in type II superconductors. When the external magnetic field is increased from zero, the depth of the screening current increases. The Bean model [12] assumes that the density of the screening current is always equal to the critical current of the material, that is $j = j_c$. This is called the critical state. The screening current penetrates to the depth that is required to cancel the external magnetic field inside the region enclosed by the current front. In regards to Equation 1.34 in Section 1.7 the Bean model also assumes $n \to \infty$. This assumption means that there is no flux creep.

Consider an interface between a type II superconductor and vacuum, where the superconductor is a long slab with a rectangular cross section. Let the y-axis be directed along the length of the slab and the x-axis point perpendicularly into the material. Let $x = 0$ mark the interface and $\mathbf{H}(x = 0) = H_0\hat{\mathbf{z}}$. The geometry is similar to the situation in Figure 1.2, however the decay of magnetic field will be different. The screening current will be parallel to the y-axis and is assumed to be equal to j_c. Therefore Equation 1.24 becomes:

$$\nabla \times \mathbf{H} = j_c\hat{\mathbf{y}}, \tag{1.35}$$

From the definition of the curl, Equation 1.35 implies that

$$\begin{aligned} j_c &= \frac{\partial H_x}{\partial z} - \frac{\partial H_z}{\partial x} \\ H_x = 0 \Rightarrow j_c &= -\frac{\partial H_z}{\partial x} \\ \Rightarrow \mathbf{H}(x) &= (H_0 - j_c x)\hat{\mathbf{z}} \end{aligned} \tag{1.36}$$

The value of $\mathbf{H}$(x) is the magnetic field corresponding to the density of flux threads and is therefore a macroscopic quantity. As the density of vortices decreases as a function of x, the magnetic field also decreases with x. The decrease in density of vortex currents make their collective current $\mathbf{j}$ nonzero. If the density was uniform, the vortex currents would cancel each other on the macroscopic length scale.
Equation 1.36 is valid for $0 \leq x \leq a$ where a is the depth where the magnetic field becomes zero, $\mathbf{H}(x = a) = 0$:

$$\mathbf{H}(a) = (H_0 - j_c a) = 0 \Rightarrow a = H_0/j_c. \tag{1.37}$$

If the applied field is sufficiently strong, the vortices will enter the whole sample. This situation is called full field penetration. Because the screening current has constant

density within depth a, the streamlines shall have constant spacing.

We can use the Bean model for other geometries than a long slab, but the thickness will remain uniform. Figure 1.4 shows the Bean model streamlines for a rectangular slab of uniform thickness. The streamlines are drawn using a computer algorithm which we discuss in Section 3.1. Notice that the streamlines must make a 90^o turn in the corners in order maintain constant spacing. If we, for each corner, draw a diagonal line through the kink of the each streamline we end up with a straight diagonal lines. This type of lines are called *D-lines*. Because the current turns abruptly we get extra screening of magnetic field on the D-line. For a square sample, the D-lines are equal to the diagonals of the square. These diagonal lines give the letter D in the name for D-lines. On the D-lines we have a magnetic field profile that is very different from the linear profile used in the Bean model, Equation 1.36. D-lines can occur in many other geometries and the

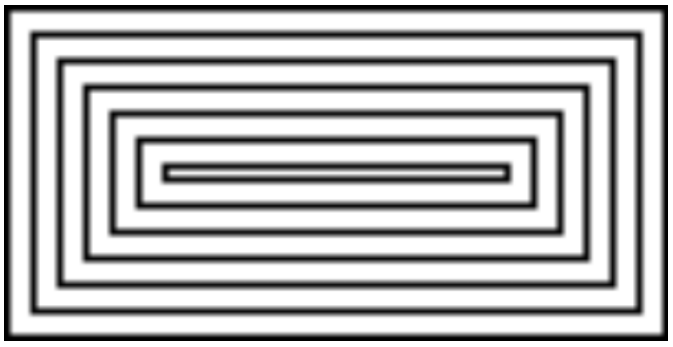

Figure 1.4: Bean model streamlines for a rectangular slab.

current kinks can be any angle, not only 90^o.

1.9 Superconducting films

Just like the distinction between type I and type II superconductors is important, we also have to make a distinction between the properties of bulk superconductors and thin film superconductors. The critical state in thin films do not have a current front, only a magnetic flux front. Still the area that is enclosed by the flux front has zero magnetic flux. Also the current will not necessarily reach the critical current. The only situation where we can assume good agreement with the Bean critical state model is for full magnetic field penetration of the sample. In that case the current is forced to reach J_c everywhere. Some analytic solutions exist for the profiles of current and magnetic field in infinitely long films of constant width [13].

When applying a magnetic field perpendicular to the film, the flux lines in the film will not generally point in the z-directions at the surface. The flux lines will have a small component parallel to the plane, directed towards the center of the film. Examples of practical applications of superconducting films are superconducting tapes [14] and

SQUID-magnetometers [15]. This thesis is dedicated to thin film superconductors of type II.

1.9.1 Electrodynamics in superconducting films

In thin films we use the sheet current $\mathbf{J}$ instead of the current density j. The sheet current is equal to the z-integral of the current density:

$$\mathbf{J}(x,y) = \int_0^d \mathbf{j}(x,y,z)dz, \tag{1.38}$$

where d is the thickness of the film. For films we define the z axis to be normal to the film and $z = 0$ corresponds to one of the surfaces. The x and y axis span the plane of the film. If d is very small we can write

$$\mathbf{j} = \mathbf{J}\delta(z). \tag{1.39}$$

where $\delta(z)$ is the delta-function.
In films it is common and convenient to work with the local magnetization $g(x,y)$ which is defined as [8]

$$\mathbf{J}(x,y) = -\hat{\mathbf{z}} \times \nabla g(x,y) = \nabla \times \hat{\mathbf{z}} g(x,y). \tag{1.40}$$

$g(x,y)$ is zero outside the film. Inserting Equation 1.40 into Equation 1.39 we get

$$\mathbf{j} = \nabla \times (\hat{\mathbf{z}} g(x,y))\delta(z). \tag{1.41}$$

Because of the cross product in Equation 1.40, we see that the sheet current is orthogonal to the gradient of g. Because both vectors are in the xy-plane we can conclude that the streamlines of $\mathbf{J}$ must be parallel to the contour lines of g. This fact is useful when we want to plot the streamlines of the current field.

Inserting 1.41 into Equation 1.24 we get

$$\nabla \times \mathbf{H}(x,y,z) = \mathbf{j} = \nabla \times (\hat{\mathbf{z}} g(x,y))\delta(z). \tag{1.42}$$

$\mathbf{H}$ can be calculated by inverting Equation 1.42. Note that the displacement current has been neglected and that $\mathbf{H}$ is only the self field of the superconducting currents. If an external magnetic field $\mathbf{H}_a$ is applied, the total field will be the superposition of the two fields.

We assume that the electric field averaged over the thickness of a superconducting film is

$$\mathbf{E}(x,y) = \rho \mathbf{J}(x,y)/d. \tag{1.43}$$

Similarly to Equation 1.34 we can use a power model [16], p. 9, for the resistivity of films:

$$\rho(x,y) = \rho_0 \left(\frac{H_z}{H_{c2}}\right)^m \left(\frac{J(x,y)}{J_c}\right)^{n-1}. \tag{1.44}$$

ρ_0 is a constant and m and $n \propto T^{-1}$ are material constants. Given a relatively high value of n like 10 or 100, we see that the resistivity becomes large when the current grows above the critical current. The term

$$\left(\frac{H_z}{H_{c2}}\right)^m$$

has little influence on the resistivity [16]. If we neglect it we get

$$\rho(x,y) \approx \rho_0 \left(\frac{J(x,y)}{J_c}\right)^{n-1}. \tag{1.45}$$

This is the resistance for $J < J_c$ and $T < T_c$. The time derivative of $\mathbf{H}$ was stated in Equation 1.26 as

$$\dot{\mathbf{H}} = -\frac{1}{\mu_0}\nabla \times \mathbf{E} = -\frac{\rho}{\mu_0 d}\nabla \times \mathbf{J}(x,y), \tag{1.46}$$

where we inserted Equation 1.43. Further substitution of $\mathbf{J}$ by Equation 1.40 yields

$$\dot{\mathbf{H}} = -\frac{\rho}{\mu_0 d}\nabla \times (-\hat{\mathbf{z}} \times \nabla g(x,y)) \tag{1.47}$$

By using the definition of the triple vector product

$$\mathbf{a} \times (\mathbf{b} \times \mathbf{c}) = \mathbf{b}(\mathbf{a} \cdot \mathbf{c}) - \mathbf{c}(\mathbf{a} \cdot \mathbf{b}),$$

we can write the time derivative of the self field as:

$$\dot{\mathbf{H}} = -\frac{\rho}{\mu_0 d}((-\hat{\mathbf{z}})(\nabla \cdot \nabla g(x,y)) - \nabla g(x,y))(\nabla \cdot (-\hat{\mathbf{z}})) = \frac{\rho}{\mu_0 d}(\nabla \cdot \nabla g(x,y))\hat{\mathbf{z}} \tag{1.48}$$

For a given state $g(x,y,t)$ we can calculate $\mathbf{H}(t)$, $\dot{\mathbf{H}}(t)$, $\mathbf{J}(t)$ and $\mathbf{E}(t)$. In other words $g(x,y,t)$ describes the state of the superconductor and by numerical time integration of $\dot{\mathbf{H}}(t)$ we can find the state $g(x,y,t+\Delta t)$.

1.10 Protocols for the applied magnetic field

The externally applied magnetic field is a central parameter in superconductor research. In this thesis we will only apply the field perpendicularly to the film. For experiments we need to cool the sample to a temperature below T_c. When we reach T_c we must record both the magnitude and direction of the external magnetic field. *Field cooling* is when the external field is non-zero during cooling. If the field is zero we call it *zero field cooling*. In this thesis we will only consider zero field cooling. When the sample has transitioned to the superconducting state and the desired temperature has been reached, we can start varying the external magnetic field. The process of changing the external field is called a ramping protocol. The simplest ramping protocol is increasing (or decreasing) the magnetic field at a constant rate until we reach the desired value. We can make more sophisticated ramping protocols by combining simpler ones. An example is shown in Figure 1.5(a). This ramping protocol is used to measure the magnetization curve for superconductors of type II.

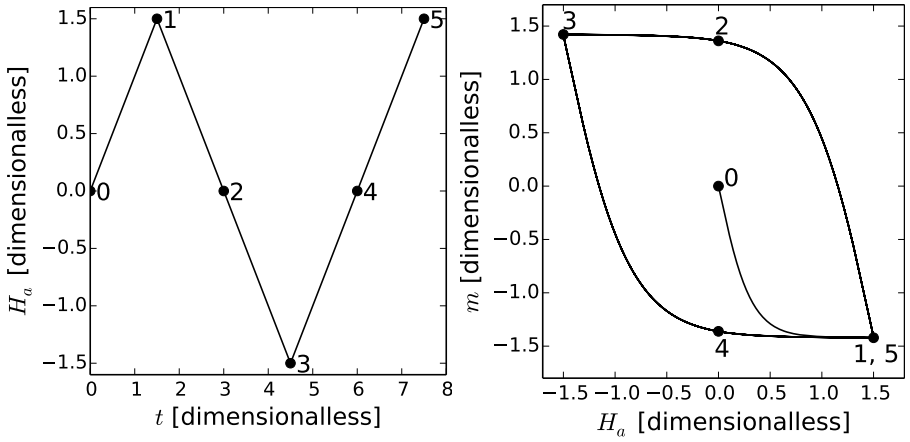

(a) Ramping protocol for hysteresis. The numbered dots indicate states for later reference.

(b) The magnetization curve resulting from the ramping protocol in Figure 1.5(a)

Figure 1.5: Ramping protocol for hysteresis and the resulting magnetization.

In this section we will use results from numerical simulations on square films to demonstrate the magnetization curve of a superconductor of type II. The mathematical formalism, implementation and dimensionalless units are explained in Section 3.2.

Consider a superconducting film of type II that has been zero field cooled. We will now apply the field ramping protocol illustrated by Figure 1.5(a). The numbers correspond to the numbered states in Figure 1.5(b). Let us comment on the numbered magnetization states along the hysteresis loop:

0. The sample has no magnetic field history. This state is called the *virgin state*.

1. The sample has been exposed to certain maximum value in applied magnetic field, $H_{a,1} = H_{a,max}$.

2. The external field is turned back down to zero. The sample is in the *remnant state*.

3. The sample has been exposed to some a certain value $H_{a,3} = -H_{a,max}$. The properties in this state are anti-symmetric to state 1, that is $g_3(x, y) = -g_1(x, y)$.

4. The sample is back in a remnant state that is anti-symmetric to state 2.

5. This state is equal to state 1 even though the magnetic field history is different.

Figure 1.5(b) is actually the simulation results of applying six cycles of the ramping sequence 1-4 in Figure 1.5(a). The magnetization curve appears to overlap itself perfectly and we cannot see any sign of accumulated numerical error. The magnetization curve shows hysteresis just like a ferromagnet. The sign of the magnetization is however opposite of the magnetization that a ferromagnet would have. It is important to note that the shape of the hysteresis loop would be different if the local critical sheet current density was a function of the local magnetic field [17].

In this thesis we will mainly study samples in the state of full penetration of magnetic field, which corresponds to number 1 in Figure 1.5. In our computer simulations we cannot reach the ideal state of full penetration. However we can realize a state where the magnetic field penetrates *almost* all parts of the sample. The results from such a simulation has been shown in Figure 1.6. At full penetration the D-lines become well defined and the angle between the edge and the D-lines are 45 degrees. We can see that the magnetic field penetrates everywhere except at the D-lines. Through the middle of Figure 1.6(a) we have drawn a dashed line. The values for the magnetic field are sampled along the line and plotted in Figure 1.6(c). The two edges of the sample are located at the peak values. The external field was $\tilde{H} = 1.5$ (dimensionless) and we see that outside the film, close to the edge, the actual field is larger than the externally applied field, in this case it means $H > 1.5$. There is a region in the middle of the field profile where the field is zero. This region corresponds to the dark region in the center of Figure 1.6(a).

In Figure 1.6(b) we have plotted the magnitude of the current distribution:

$$\tilde{J}(x, y) = \sqrt{J_x^2(x, y) + J_y^2(x, y)}/J_c.$$

The dashed line in the figure corresponds to the sampling points used to plot the current profile in Figure 1.6(d). We can see that the current only reaches the critical current ($J/J_c = 1$) at the edge of the sample. The current decays slowly from the edge and into the film. Closer to the middle of the sample it falls dramatically and reaches zero at the singularity in the center. From this we can see that there is no front in the current

distribution. There is only a front in the magnetic field distribution, which reaches zero far into the film.

Because of the symmetry of the square film, the current is perpendicular to the dashed line in Figure 1.6(d). If we integrate the current profile in Figure 1.6(d) from the edge to the center of the sample, we get the flux of the circulating current. We can in principle calculate the current flux from any profile from the center to the edge of the sample. However we must make sure that only the component of the current that is perpendicular to the line is included in the calculations. The line along a D-line, from the center to the corner, will be longer than any other line we can draw from the center of the film to the edge. The extra length results in a lower sheet current because the flux is distributed along a longer line. We can see the reduction in sheet current along the diagonals in Figure 1.6(b).

Figure 1.6(d) ignores the direction of the current because it is a plot of the magnitude, $|\mathbf{J}|$. For the current across the dashed line it is easy to include the sign because it is simply the y-component of the current $\mathbf{J_y}$. We plot the profile of $\mathbf{J_y}$ in 1.6(e) and see that it is asymmetric about the center. This is expected from the rotational symmetry of the current field, circulating in the sample.

Both profiles of magnetic field and sheet current are useful tools to study results from simulations. The profiles through the middle of the sample, perpendicular to the edges, are the easiest to interpret and are the only form of profiles studied in this thesis.

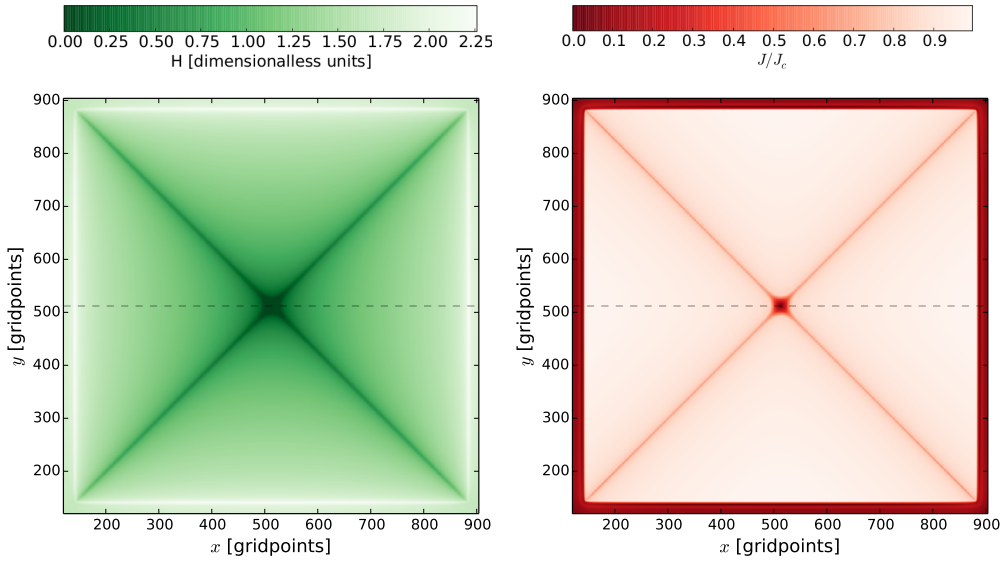

(a) Full field penetration magnetic field penetration of a square sample.

(b) The distribution of the *magnitude* of sheet current, corresponding to the magnetic field in Figure 1.6(a).

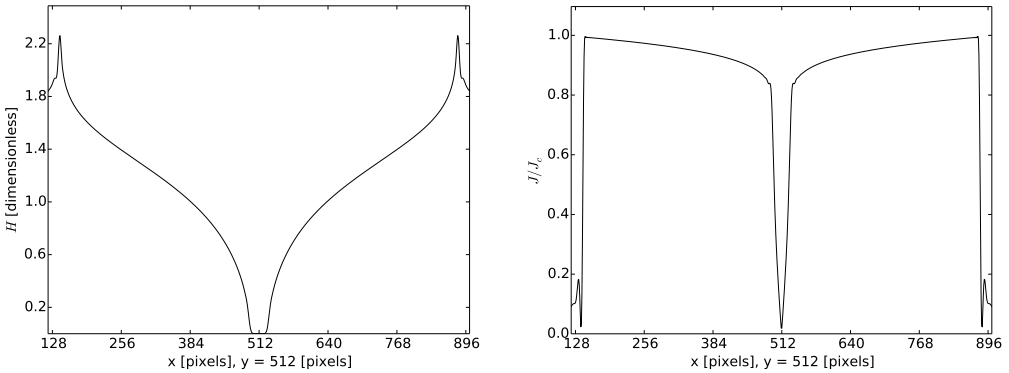

(c) Field profile through the dashed line in Figure 1.6(a)

(d) Profile of the *magnitude* of current measured on the dashed line in Figure 1.6(b)

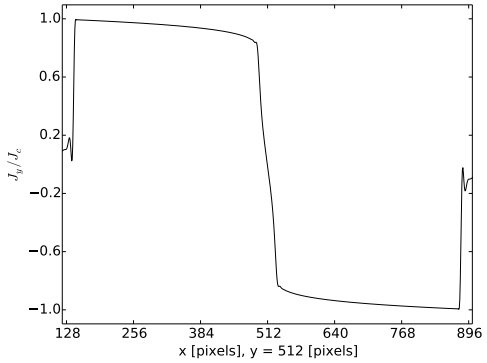

(e) profile of the current across the dashed line in Figure 1.6(b)

Figure 1.6: Profile of the current measured along the dashed line in Figure 1.6(b).

1.11 Dendritic flux avalanches

In type II superconductors we can get various types of magnetic flux jumps and flux flux avalanches. With this we mean that magnetic flux enters the superconductor in an abrupt manner. Magneto-optical imaging [18] can be used to study the magnetic field distribution resulting from such phenomena. Some flux avalanches create flux patterns that look like a tree branch. In science such tree-like patterns are called dendritic patterns. The word "dendritic" is derived from the greek word déndron, which means tree. Therefore we call the tree-like flux avalanches for *dendritic flux avalanches*. In the lingo they are called "dendrites". While such avalanches are produced in a very short time, the resulting flux pattern stays for a very long time. That is unless we increase the applied field so that the dendrite gets erased by the invading flux front. An example of dendrites imaged using magneto-optical imaging has been shown in Figure 1.7(a). The bright horizontal line in the upper part of the figure is the north edge of the sample. From there we can see two dendritic patterns of magnetic flux. They appeared after increasing the applied magnetic field from zero to 13.6 mT. The experiment was conducted at a temperature of 3.7 K. On the left side of the image we also see parts of a third dendrite. In this particular case of dendritic avalanches, the branches are relatively straight. At other temperatures the branch pattern may become more or less dense and/or angular.

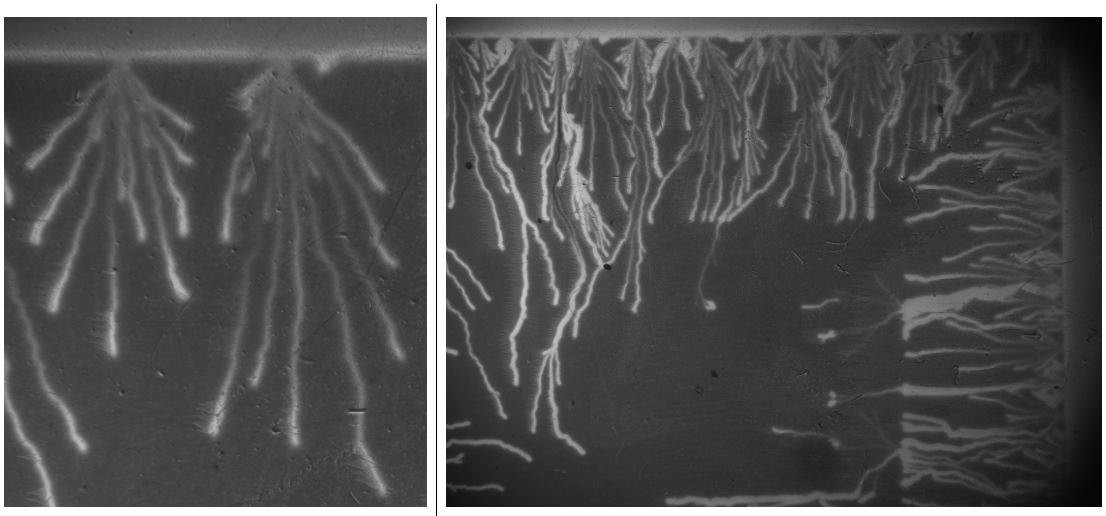

(a) Dendrite in superconducting NbN film. Brightness represents strong magnetic field relative to the dark areas, where the field is weak.

(b) Dendrites in NbN with pressed aluminium frame. The applied field was 25.5 mT.

Figure 1.7: Examples of dendrites in an NbN superconducting film using magneto-optical imagning. The images are original images by the author. Thanks to Thomas Qureishy for assisting in the experiment.

For a MgB_2 film it was shown [19] that more dendrites were formed at low temperatures (3.3 K) compared to higher temperatures(9.9 K). However the dendrites formed at higher temperatures had more branches. At 10.5 K there were no dendrites and this confirms that there is an upper threshold temperature for dendritic avalanches. In [19] we can also read about how dendrites demagnetize the samples. The threshold temperature was also found for pure niobium [20]. The latter paper shows dendrites appearing when the applied field is turned back down to zero, approaching the remnant state. The paper also shows images of the individual vortices in the dendrites using magnetic Bitter decoration.

In [21] it was shown that narrow strips (0.2 mm) are more resistant to nucleation of dendrites than wider ones. For a given sample the dendrites often have favorite starting points and favorite branching patterns corresponding to the different starting points. Therefore similar dendrites can happen over and over during an experiment.

It is possible to avoid dendritic avalanches by covering the superconducting film with a metal layer. Paper [22] reports on an experiment where an aluminium disk was placed in a range of vertical distances($0 - 450\,\mu m$) above the surface of superconducting films. For MgB_2 and Nb films the aluminium disc suppressed dendritical avalanches. The closer the disk was to the film, the better the stability became. Direct contact between the metal and the film was not necessary to observe increased stability. However the stability became excellent when the metal was is in direct contact with the film. Figure 1.7(b) is a magneto optical image of the same NbN as in Figure 1.7(a), but shows a larger part of the sample and because the field is stronger it shows many more dendrites. If one looks closely at the top left corner, it is possible to see the two dendrites from Figure 1.7(a). The sample in Figure 1.7(b) has a rectangular aluminium foil frame pressed on top of it. The frame itself is not visible in the magneto-optical image, but the north and east edge are indicated quite sharply by the absence of dendrites. The result is that the dendrites that propagate in the covered region are weakened. This effect has been known for several years [23] and is caused by both electromagnetic breaking and heat conduction. Notice that some dendrites are powerful enough to reach inside the frame. This means that dendrite protection cannot be guaranteed which in turn limits the practical applications of such frame protection. On the bottom of the figure we see a dendrite that runs parallel to the edge of the metal frame. The figure is therefore an example of the fact that metallic layers can both weaken and lead dendrites. Metal layers of gold can also be used to protect against dendrites. This was demonstrated in [24]. An MgB_2 film was covered with gold along half its circumference. The result was suppression of dendrites where the edge was covered. The edges which were not protected by gold edges showed many dendrites. The thicker the gold layer, the higher external field was needed to make dendrites penetrate into the protected region.

When there are more than one dendrite, the dendrites tend to avoid each other so that the branches of the dendritic patterns do not cross. This was one of the first phenomena discovered in magneto optical imaging of dendritic flux avalanches [25].

The growth speed of an avalanche is hard to determine in experiments because they happen on a very short time scale. Paper [26] reports on dendrites nucleated artificially in an YBCO sample. By using a laser pulse, the temperature was raised in a small area of the film. This triggered both a dendrite and a camera. The camera recorded magneto optical images at various time delays after the dendrite nucleation. The propagation speed was found to decrease during the avalanche. In the beginning of the avalanches the speed was found to be strongly dependent on the applied field. the average speed after a 4.2 ns delay were about 125 km/s for $H_a = 12.7$ mT and about 250 km/s for $H_a = 20.6$ mT [2]. Towards the end of the avalanche, after a 37.7 ns time delay, the average speeds were about 25 km/s and 20 km/s. Dendritic avalanches with anisotropic propagation was investigated in [27].

Dendritic avalanches are important because they destroy the local superconducting state and thus limits the supercurrents. Their direction of propagation is toward the center of the sample, crossing the current streamlines. They can appear when the field is increased, but also when the field is reduced back to zero. As temperatures and fields are important, one can make scatter plots of dendrites as function of temperature and field.

From a theoretical point of view we consider the time dependent critical current density J_c. As the local temperature in a superconductor fluctuates, the critical current will fluctuate as well. If the critical current fluctuation leads to J_c being smaller than the local current density, there will be a local transition to the normal. In the normal state the current will produce heat which causes the surrounding superconductor to heat up as well. Therefore the surrounding material can exit the superconducting phase. This process becomes a feed back loop and is what triggers dendritic flux avalanches. The mechanism behind the propagation of dendritic flux avalanches is understood.

[2] The numbers are read from a graph in the paper and are therefore only approximates.

Chapter 2

2. Inhomogenous superconductors

2.1 Manipulation of the critical sheet current

In this thesis we treat the critical sheet current of a film as an isotropic quantity. In many materials the critical sheet current J_c scales with the thickness of the material. Now consider a superconducting film of uniform thickness d_0. The uniform thickness leads to a uniform critical sheet current J_{c0}. If we change the thickness in a given region from d_0 to d_1, we expect the critical current density to change to

$$J_{c1} = \frac{d_1}{d_0} J_{c0}. \tag{2.1}$$

If the thickness is halved in the region, then

$$\frac{d_1}{d_0} = 0.5 \Rightarrow J_{c1} = \frac{1}{2} J_{c0} \tag{2.2}$$

The flux of current from the unperturbed to the perturbed region is limited yo the lowest critical sheet current density of the two regions. These types of discontinuous transitions to lower or higher J_c has been discussed in [18]. In Figure 2.1 the current approaches the region of reduced thickness (the gray area) at some angle α. The local sheet current is assumed to be equal to the local critical current, as we can assume for a film at full magnetic field penetration. When

$$J = J_{c0} > J_{c1},$$

the angle α must obey

$$J_{c1} = cos(\alpha) J_{c0}$$

in order for the local critical sheet current to be equal to the local critical sheet current.

Let us consider a rectangular superconducting slab with reduced thickness along a stripe across the sample. We call this region a channel and for simplicity we choose the

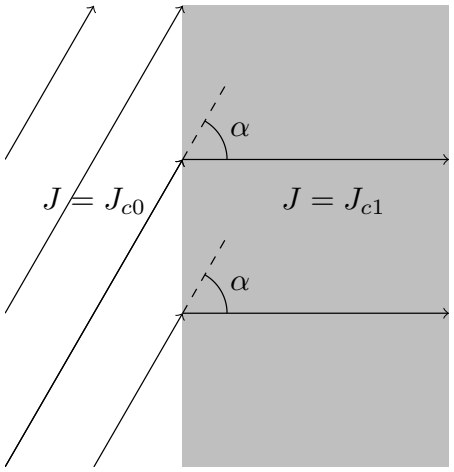

Figure 2.1: Critical sheet current crossing the boundary to lower critical sheet current, which is marked in gray.

film thickness in the channel to be half of the film thickness in the rest of the sample. We assume that this reduces the critical current density by half in the channel and that the current density in the channel reaches half of the original critical current density, $j = \frac{1}{2} j_{c0}$. The applied magnetic field is increased until we reach full field penetration. Right next to the channel, the current density will not be able to reach the local critical current density. This is because the current density must be adjusted in order to transition to the region of lower current density. The algorithm, discussed in Section 3.1, returns the streamlines shown in Figure 2.2. Notice that we have D-lines where the current enters and leaves the channel. If we study the part to the right of the channel and the one to the left of the channel separately, we can see D-lines from each corner. We also see a horizontal D-line which starts in the middle of the channel. The latter is an example of a D-line where the current kinks are not 90^o. This current streamlines are qualitatively similar to the current streamlines drawn for the weak link in [18], where the extra D-lines lead to additional lines of increased screening of magnetic field.

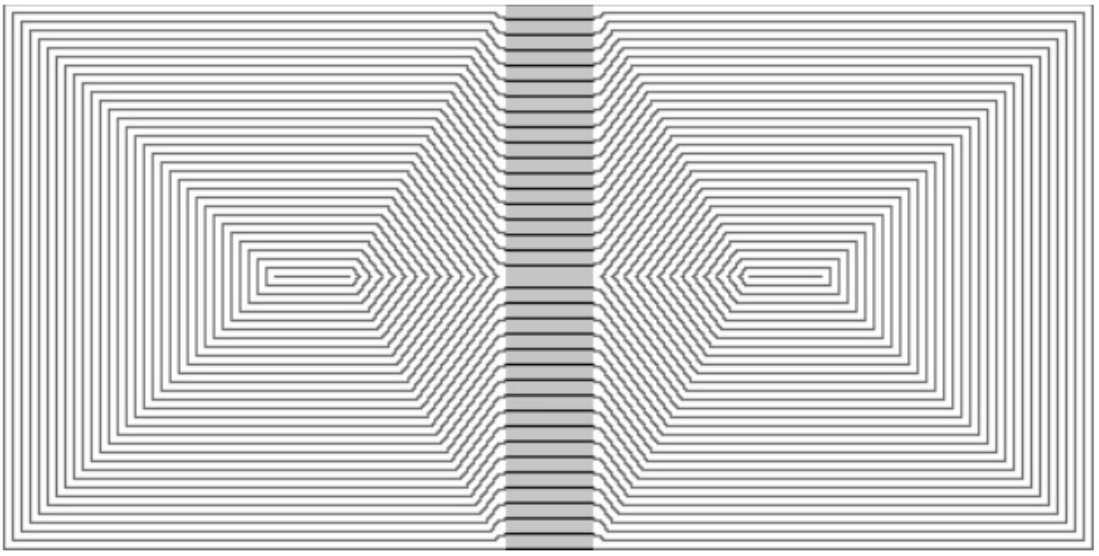

Figure 2.2: Using the algorithm on a sample with 50% reduction of J_c in a stripe going through the middle of the sample.

In Figure 2.3 we have stacked rectangular regions of J_{c0} and J_{c1} side by side and drawn the corresponding screening currents. Only the south edge of the film is visible in the figure and therefore we have only drawn current streamlines from the south edge. We have required the sample to be at full magnetic field penetration so that the Bean model is valid. Then the streamline density will be inversely proportional to the local current density. We have already explained how the regions of reduced critical sheet current dictate the direction of the current field near the region(see Figure 2.1). The rectangles of reduced J_c will be called *channels* and their width is named c. The width of the unperturbed rectangles are named b. We can, in theory, make a sample with many parallel channels. The component of the current that runs perpendicular to the channels

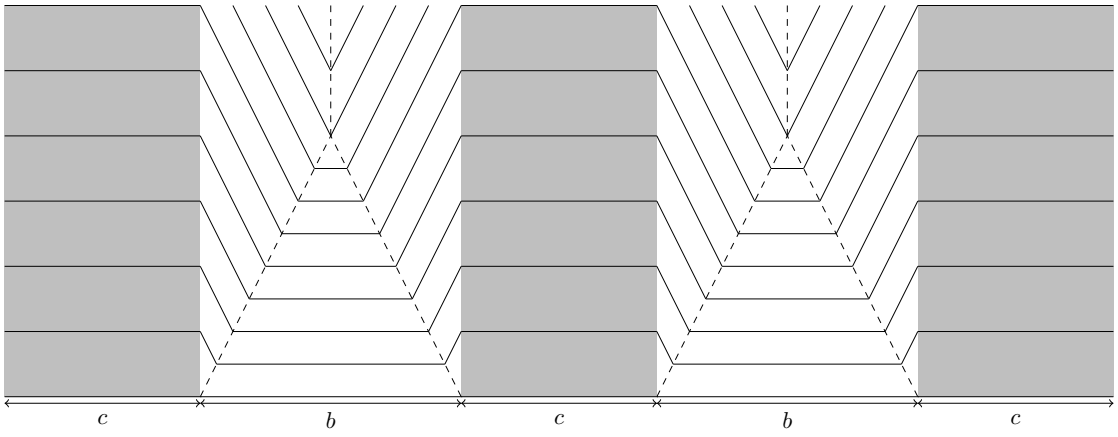

Figure 2.3: Streamlines of current in alternating high and low critical current regions, with Bean model assumptions. The superconductor is assumed to continue to the sides and in the upwards direction. The bottom edge of the figure marks the edge of the sample.

will have the upper limit J_{c1}. The component running parallel to the channels will be limited to the local value of J_c, which can be either J_{c1} or J_{c2}. From these assumptions it seems like such a sample will have anisotropic properties on a length scale that is comparable to the size of the sample.

2.2 Anisotropy

2.2.1 Traditional anisotropy

Traditional films with anisotropic screening currents [27] show the current pattern in Figure 2.4. In the case of anisotropic samples, the D-lines are not angled 45 degrees relative to the sample edges. We also see that the D-lines divide the samples into four regions.

- One triangle in the west part of the sample.
- The equivalent triangle on the east part of the sample.
- A trapezoid in the northern part.
- The equivalent trapezoid in the southern part.

The current field is stronger in the triangles on the west and east side. In these regions the current is flowing parallel to the axis of high critical sheet current. In the north and south trapezoids the current is flowing parallel to the axis of lower critical sheet current. In order for the flux of current to be equal through all the regions, the regions of denser current must have a smaller width:

$$\Delta x J_y = \Delta y J_x \tag{2.3}$$

This is the reason for the trapezoid shape for the high current regions.

2.2.2 Manufactured anisotropy

With the current flow in Figure 2.4 fresh in mind we can construct a first approximation for how current will flow in a sample with channels. We are ultimately interested in how the current field looks on much larger length scale than the period of the channel pattern, $b + c$. The fine structure of the currents, shown in Figure 2.3, becomes less important at the macroscopic scale. We consider a sample with dense channels across the sample in the north-south direction. We expect the current across the channels to be less dense so that the sample will show trapezoidal regions in its north and south part. In these regions the current vector is parallel to the x-axis and the sheet current reaches

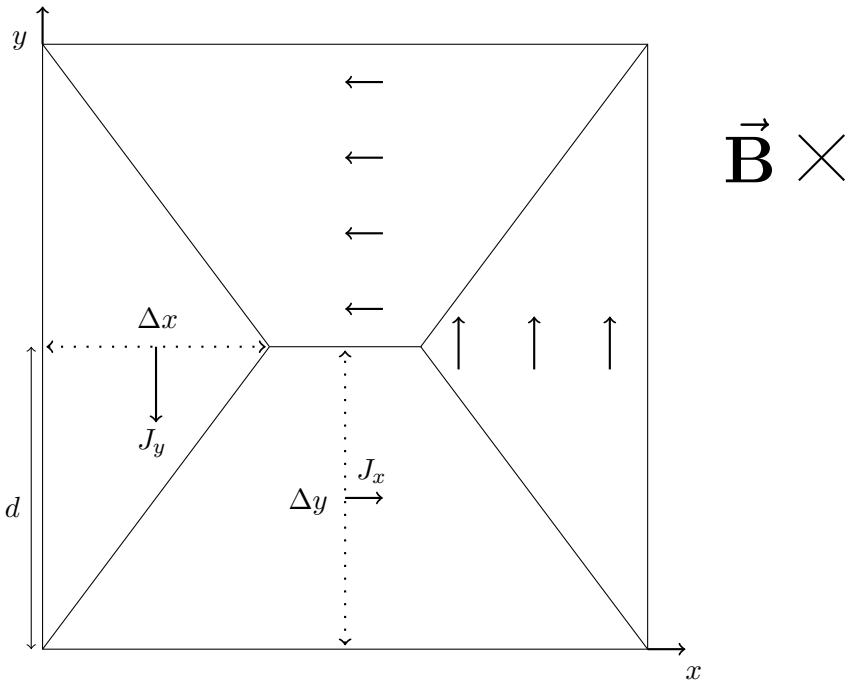

Figure 2.4: An ideal anisotropic sample at full magnetic field penetration. The square represents a superconducting film and the solid lines drawn on the inside represent the D-lines at full penetration. The applied magnetic field $\vec{B}$ is directed into the plane. The diagonal lines are the D-lines. Δx marks the depth of the triangles in the western and eastern regions. Δy marks the depth of the trapezoids in the north and south regions. d is the half width of the square sample. The unnamed arrows represent the current density vector field. Their relative spacing and length indicate that $J_y > Jx$.

the critical sheet current in the channels:

$$J = J_x = J_{c1}. \tag{2.4}$$

In the triangular regions in the west and east part we assume that the current is flowing parallel to the y-axis. The sheet current in these regions should be the average critical sheet current. With this we mean the weighted sum of the two critical sheet currents J_{c1} and J_{c2}, divided by the period $b + c$ of the channel pattern:

$$J = J_y = (J_{c0} \cdot b + J_{c1} \cdot c)/(b + c) \tag{2.5}$$

If we introduce

$$B \equiv \frac{b}{b+c} \quad , \quad C \equiv \frac{c}{b+c}$$

then 2.5 can be simplified to

$$J_y = BJ_{c0} + CJ_{c1} \tag{2.6}$$

Using the symbols in figure 2.4 we define the anisotropy factor by dividing Equation 2.5 on Equation 2.4:

$$a = J_y/J_x = (BJ_{c0} + CJ_{c1})/J_{c1} = BJ_{c0}/J_{c1} + C \tag{2.7}$$

Because we are interested in the ratio between the currents, we can use dimensional units for J_{c0} and J_{c1}. Normalizing J_{c0} to unity we get

$$\begin{aligned} a &= B/J_{c1} + C \\ J_x &= J_{c1} \\ J_y &= B + CJ_{c1} \end{aligned} \tag{2.8}$$

The simplest case is when $b = c$. In that case we get:

$$\begin{aligned} B &= C = 1/2 \\ J_x &= J_{c1} \\ J_y &= (1 + J_{c1})/2 \\ a &= (1/J_{c1} + 1)/2 \end{aligned} \tag{2.9}$$

From Equation 2.3 we have that

$$\Delta x J_y = \Delta y J_x \Rightarrow \Delta y/\Delta x = J_y/J_x \Rightarrow a = \Delta y/\Delta x \tag{2.10}$$

When an anisotropic sample has been ramped up to full magnetic penetration we can use the expression for $a = \Delta y/\Delta x$ to find the anisotropy factor.

Chapter 3

Numerical methods

3.1 Algorithm for plotting Bean model streamlines

We are sometimes interested in the streamlines of shielding current in superconducting samples. For theoretical studies it is common to assume a Bean model for the current, where the streamlines are equidistant. We must decide on a distance between the streamlines. Let us call this distance d. If the distance is too large, the fine structure in the streamlines will be lost. If the distance is too small the number of lines will be large. Then it will take a long time to draw the streamlines. The starting point of an analytic drawing is to draw a streamline along the boundary. This is the first streamline. From the requirement of equidistant streamlines we know that the next streamline must be exactly at a distance d from the first streamline. In principle we can use a compass to draw arcs of radius d around points on the first streamline. This has been done in Figure 3.1(a), where the arcs have the dashed line-style. Because the streamlines must

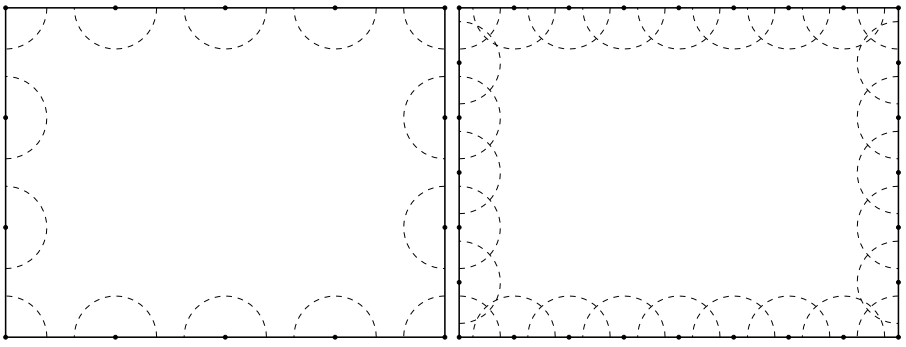

(a) Drawing arcs with uniform radius around selected points along the streamline along the border.

(b) Increased number of points for which arcs are drawn.

Figure 3.1: Drawing Bean model streamlines manually using a compass.

be equidistant we have the two conditions for the next streamline:

- It must be drawn on the arcs.

- No part of it may be inside an arc.

The set of points where these two conditions are fulfilled will approximate a streamline when we draw many arcs. In Figure 3.1(b) we have drawn more arcs than in Figure 3.1(a). We see that the points that fulfill the conditions in 3.1 form a squiggly line. If we draw an infinite number of arches, then this line will be much smoother and we will be able to draw the next streamline from this line. Of course this method involves a lot of work. It is also not necessary for the simple geometry of a rectangular sample; we know that the streamlines will be concentric rectangles.

The reason that we present this rather laborious method is that it can be done quickly by a computer. The iterative process of drawing streamlines is shown in Figure 3.2. We start out with a matrix representation of the sample. The matrix elements can have values 0 or 1. Because it only stores these two values we will name it the *boolean matrix*. The boolean matrix tells us if a coordinate in the sample is inside a radius d of some point on the existing streamlines or not. If the value is zero it means that the coordinates are too close to existing streamlines, which in turn tells the computer that no streamlines can be drawn through the element. An element with value 1 means that it is not too close and therefore it may be possible to draw a streamline through the coordinates corresponding to the element. To store information about where the streamlines have been drawn, we use a streamline matrix. This matrix can store two values: 0 and 1. 0 means that the streamlines do not go through the element. 1 Means that there is a streamline that goes through the element. We start out with a boolean matrix where every element has value 1. This means that every point of the sample are candidates for streamlines. The streamline matrix starts out with value 1 in the first and last columns and rows. This means that we have drawn a streamline along the edge of the sample, like in Figure 3.2(a). The indices of the streamline are recorded by the computer. We have decided that the distance d between the streamlines sahll be 7 pixels. The computer iterates through every element in the streamline matrix where the streamline was drawn. Every element in the boolean matrix that is closer than d to the current element on the streamline is set to zero:

$$\sqrt{\Delta x^2 + \Delta y^2} < d$$

Therefore the elements containing 1 in the boolean matrix decreases. The elements that contain 1 in the boolean matrix is marked with gray in Figure 3.2(a). The elements containing 0 are white. A streamline will be drawn through the elements that are gray and has one or more neighbors that are white. These elements are at a distance d from the latest streamline. In Figure 3.2(b) we have illustrated the elements that are too close to the a specific point on a streamline using a discrete circle in gray. The process of drawing new streamlines continues until the boolean matrix only contains zeros. Then the streamline matrix is saved to a file. After the second streamline has been drawn

and the computer has eliminated invalid elements in the boolean matrix we are left with the tiny gray rectangle marking the possible streamline elements in Figure 3.2(c). From this the last streamline is drawn in the center of Figure 3.2(d). The last streamline demonstrates a problem: The last streamline is too close to itself and should therefore not be included. If we had chosen a different distance between the streamlines we might not have ended up with this problem. One option is to do a second simulation where we change d to some other value. Another option is to erase the last streamline.

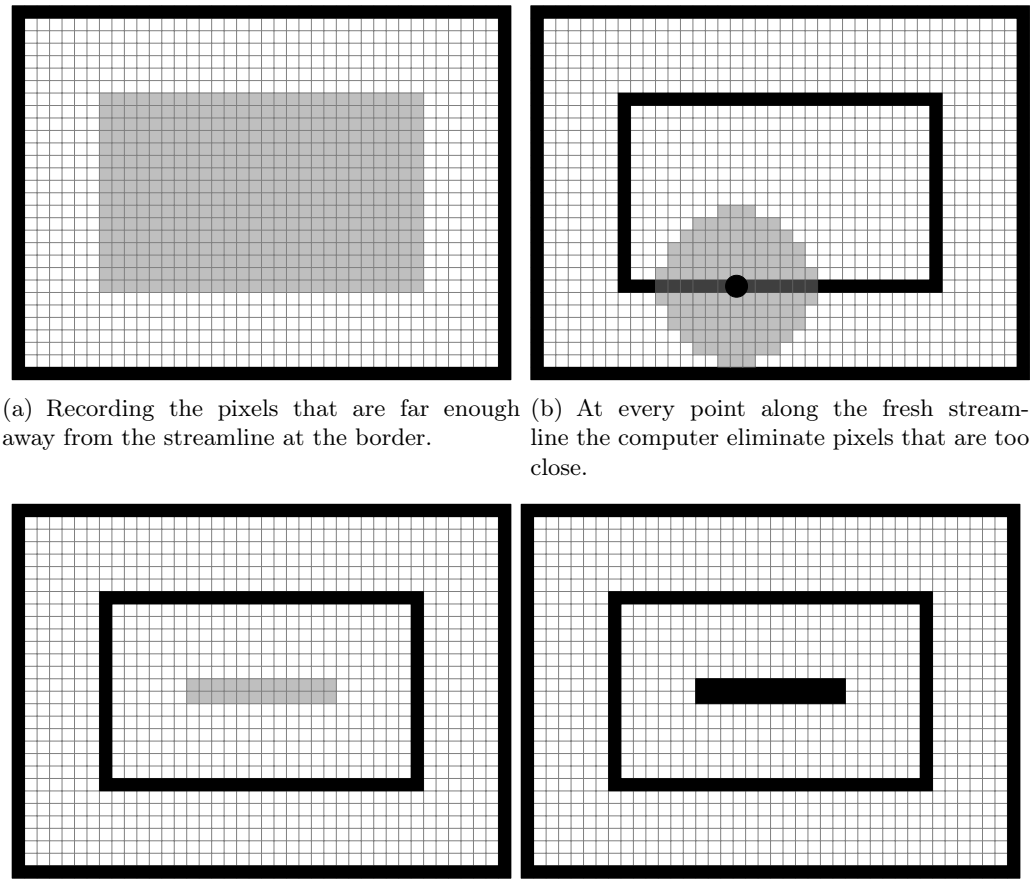

(a) Recording the pixels that are far enough away from the streamline at the border.

(b) At every point along the fresh streamline the computer eliminate pixels that are too close.

(c) The pixels that were not removed by the elimination are marked in gray.

(d) The last streamline has been drawn.

Figure 3.2: Drawing a new streamline

There is a usability problem in that the distance between the streamlines is rounded to the nearest pixel. Consider a sample with $J_c = 1$ and a distance 10 pixels between each streamline. If we made a perturbation in the film where $J_c = 0.900$ the distance should be $10 \text{ pixels} \cdot 0.900^{-1} \approx 11.1$ pixels. This will be rounded off to 11 pixels. For a perturbation $J_c = 0.96$ we get ≈ 10.4 pixels which will be rounded to 10 pixels. Thus the algorithm does not pick up on gradual changing critical current. We should therefore increase the distance between the lines; for example 100 pixels distance in between the streamlines. Unfortunately there will still be round off errors. If the distance between the streamlines is too large compared to the gradient of J_c, then the subtle change in

density of streamlines will not be visible. It is similar to using too large of a box width when calculating an integral by a finite sum. On one hand the distance must not be too small, but it must show enough detail. One solution is to increase the resolution of the matrices used in the program. Then the process will take a long time. Another solution is to only draw the streamlines for a selected region of the sample. In that case the initial streamlines in the program must be changed so that they do not surround the region.

The program is intended to check our intuition when drawing Bean model streamlines. The algorithm has problems with round off errors and can lead to both quantitative and qualitative errors if used incorrectly. We must therefore neither trust or disregard the output of the program. A good approach is to use the program to check our intuition.

3.2 Numerical simulations of electrodynamics in films

This section is dedicated to the mathematical formalism and numerical methods used by the simulation program for electrodynamics in superconducting films. The program was implemented by Jørn Inge Vestgården and this section is based on the description in his paper, [16].

The purpose of the simulations is to calculate the sheet current field, the magnetic field and local magnetization g as the state of the system evolves in time. In the simulations we must specify the grid resolution in the xy-plane, the creep exponent n and the protocol for ramping of the applied magnetic field H_a. The applied field is parallel to the z-axis, or in other words perpendicular to the film. One of the optional parameters is the scalar field $J_c(x, y)$ which is the local critical sheet current.

3.2.1 The relation between magnetic field and the local magnetization

The evolution of the self field of the sample depends on the screening currents. We use the local magnetization g as a representation of the screening current. It is therefore important to find the relationship between the self field and the local magnetization.

From Equation 1.42 we have a relation between $g(x, y, z)$ and $\mathbf{H}(x, y, z)$:

$$\nabla \times \mathbf{H}(x, y, z) = \nabla \times (\hat{\mathbf{z}} g(x, y))\delta(z) \tag{3.1}$$

Calculating the left hand side of the equation we get

$$\nabla \times \mathbf{H}(x, y, z) = \left(\frac{\partial H_z}{\partial y} - \frac{\partial H_y}{\partial z}\right)\hat{\mathbf{x}} - \left(\frac{\partial H_z}{\partial x} - \frac{\partial H_x}{\partial z}\right)\hat{\mathbf{y}} + \left(\frac{\partial H_y}{\partial x} - \frac{\partial H_x}{\partial y}\right)\hat{\mathbf{z}} \tag{3.2}$$

The right hand side becomes

$$\nabla \times (\hat{\mathbf{z}} g(x, y))\delta(z) = \begin{vmatrix} \hat{\mathbf{x}} & \hat{\mathbf{y}} & \hat{\mathbf{z}} \\ \frac{\partial}{\partial x} & \frac{\partial}{\partial y} & \frac{\partial}{\partial z} \\ 0 & 0 & g(x, y) \end{vmatrix} \delta(z) = \delta(z)\left(\frac{\partial g(x, y)}{\partial y}\hat{\mathbf{x}} - \frac{\partial g(x, y)}{\partial y}\hat{\mathbf{y}}\right) \tag{3.3}$$

By setting each dimension in Equation 3.2 equal to the same dimension in Equation 3.3 we get the following set of equations:

$$\begin{aligned} \left(\frac{\partial H_z}{\partial y} - \frac{\partial H_y}{\partial z}\right) &= \delta(z)\frac{\partial g(x, y)}{\partial y} \\ \left(\frac{\partial H_z}{\partial x} - \frac{\partial H_x}{\partial z}\right) &= \delta(z)\frac{\partial g(x, y)}{\partial y} \\ \left(\frac{\partial H_y}{\partial x} - \frac{\partial H_x}{\partial y}\right) &= 0 \Rightarrow \frac{\partial H_y}{\partial x} = \frac{\partial H_x}{\partial y} \end{aligned} \tag{3.4}$$

For a non-magnetic material, the divergence of magnetic field is zero:

$$\nabla \cdot \mathbf{H} = \frac{\partial H_x}{\partial x} + \frac{\partial H_y}{\partial y} + \frac{\partial H_z}{\partial z} = 0 \tag{3.5}$$

It is inconvenient to use partial derivatives and therefore the simulation algorithm works with the Fourier form of the equations. The Fourier transform is defined as

$$\hat{f} = \mathcal{F}[f] = \int_{-\infty}^{\infty} f \exp(-ikx) dx \tag{3.6}$$

Where $\hat{f}$ is the Fourier transform of f and k is the wave number. When transforming a partial derivative we do integration by parts:

$$\mathcal{F}\left[\frac{\partial^n f}{\partial x^n}\right] = (ik)^n \hat{f} \tag{3.7}$$

We see that the Fourier transform of a spatial derivative of a function is equal to the function times the term ik. Doing a three-dimensional transform of Equation 3.4 and 3.5, using 3.7, we get

$$\begin{aligned} ik_y H_z^{[3]} - ik_z H_y^{[3]} &= ik_y g^{[2]} \\ ik_x H_z^{[3]} - ik_z H_x^{[3]} &= ik_y g^{[2]} \\ ik_x H_y^{[3]} &= ik_y H_x^{[3]} \\ ik_x H_x^{[3]} + ik_y H_y^{[3]} + ik_z H_z^{[3]} &= 0 \end{aligned} \tag{3.8}$$

Where $H_i^{[n]}$ means the Fourier transform of field component i in n dimensions. The Fourier transform along the z-axis is simplified by the delta function $\delta(z)$. This is the reason that we have $g^{[2]}$ and not $g^{[3]}$ in Equation 3.8.

By solving the equations for $H_z^{[3]}$ and doing the inverse Fourier transform in the z-direction [16] one obtains that (after setting $z = 0$):

$$H_z^{[2]}(k_x, k_y) = \frac{k}{2} g^{[2]}(k_x, k_y) \tag{3.9}$$

where $k = \sqrt{k_x^2 + k_y^2}$. The relations between $H_z(x, y)$ and $g(x, y)$ are [16]

$$\begin{aligned} H_z(x, y) &= \mathcal{F}^{-1}\left[\frac{k}{2}\mathcal{F}[g(x, y)]\right] \\ g(x, y) &= \mathcal{F}^{-1}\left[\frac{2}{k}\mathcal{F}[H_z(x, y)]\right] \end{aligned} \tag{3.10}$$

3.2.2 Time evolution

We get the time evolution of the magnetic self field, inside the sample, from Equation 1.48. The z-component of the total magnetic field $\dot{H}_{total}$ is the superposition of the self field H_z and the applied magnetic field H_a. The time derivative of the total field becomes

$$\dot{H}_{total} = \dot{H}_z + \dot{H}_a. \tag{3.11}$$

Here $\dot{H}_a$ is the time derivative of the applied magnetic field and is called the ramping rate in experiments. The Fourier transformations in Equation 3.10 are time independent. Therefore the time derivative of g becomes:

$$\dot{g} = \mathcal{F}^{-1}\left[\frac{2}{k}\mathcal{F}[\dot{H}_z]\right] \tag{3.12}$$

Inside the sample we can use the expression for $\dot{H}_z$ in Equation 1.48. It states that

$$\dot{H}_z = \frac{\rho}{\mu_0 d}(\nabla \cdot \nabla g(x,y)) \tag{3.13}$$

In our calculations we include a finite region of vacuum outside the sample and Equation 3.13 is not valid in this region. If we used it without corrections it would lead to $\dot{g} \neq 0$ and $g \neq 0$ outside the sample. We want to remove this nonphysical magnetization of the vacuum outside the sample. Fortunately we have a good approximation for the field distribution outside the sample: The field distribution at the previous time step. This field can be used as a trail function which makes it possible to find a better approximation to the H_z outside the sample. The process of finding this field is an iterative process:

- Start out with a field that uses Equation 3.13 for the field inside the sample region. The field outside the sample is approximated by a trail function. In the first iteration we use the field at the previous time step. For the next iteration we will have found a better approximation which we then will use as the updated trail function.
- The field distribution is transformed to g using Equation 3.10.
- We construct a scalar field that is equal to g (calculated above) outside the sample and zero inside.
- This scalar field is transformed back to magnetic field. The field outside the sample is then subtracted from the trail distribution. To the resulting field we add a constant, outside the sample, which purpose is to assure that the magnetic flux be conserved. We have now obtained a field distribution which corresponds to smaller values of g outside the sample. Therefore it is better approximation to

the actual magnetic field outside the sample. If the g is sufficiently small, we are done; Maxwell's equations are solved and $g = 0$ outside the sample. If not, we must repeat the above process in order to find a better field distribution outside the sample.

Notice that the magnetic field inside the sample is unaltered; we only modify the field outside the sample.

We can find the time evolution of g and H_z by numerical integration of Equation 3.12. The simulation program uses the fourth order Runge-Kutta method. Using a variable time step is essential.

3.2.3 Dimensionless units

Paper [16] lists the dimensionalless form of the physical quantities. Spatial dimensions are eliminated using the half sample width ω. This is trivial for x and y:

$$\tilde{x} = x/\omega \quad , \quad \tilde{y} = y/\omega$$

We also have to make

$$\mathcal{F}^{-1}\left[\frac{2}{k}\mathcal{F}[f]\right] \rightarrow \frac{1}{\omega}\mathcal{F}^{-1}\left[\frac{2}{k}\mathcal{F}[f]\right],$$

in order to remove the dimension of length caused by $\frac{1}{k}$. We use the ramping rate $|\dot{H}_a|$ to scale time:

$$\tilde{t} = t|\dot{H}_a|/J_0$$

Here

$$J_0 = J_c\left(\frac{dw\mu_0|\dot{H}_a|H_{c2}^m}{\rho_0 J_c^{m+1}}\right)^{1/(n+m)}, \tag{3.14}$$

Here n and m are the exponents from the material law in Equation 3.14. In the simulation we use

$$J_c = J_{c0}(1 - T/T_c),$$

where J_{c0} is the critical sheet current at zero temperature. The only free parameters are $\dot{H}_a$, n and m. Their values have been chosen to be $\dot{H}_a = 1$, $n = 19$ and $m = 0$.

In section 2.1 we do local alterations of the critical current density. Effectively it is J_0 that is altered, not J_c. It is also important to note that reduced film thickness would introduce many effects other than reduced critical current. It is better to think of reduction of critical current as just that, a reduction in J_0.

For g and H we define

$$\tilde{g} = g/(\omega J_0) \quad , \quad \tilde{H} = H/J_0$$

3.2.4 Temperature dependence

The time evolution of temperature is essential for simulating dendrites. Whenever $J(x,y) > J_c$ or $T(x,y) > T_c$ the point (x,y) is in the normal state. For the dimensionalless resistance we have:

$$\begin{aligned} \rho(x,y) &= \left(\frac{J(x,y)}{J_c}\right)^{n-1} \quad \text{for} \quad J(x,y) \leq J_c \quad \text{and} \quad T(x,y) \leq T_c \\ \rho(x,y) &= 1 \quad \text{when} \quad J(x,y) > J_c \quad \text{or} \quad T(x,y) > T_c \end{aligned} \tag{3.15}$$

Here ρ_n is the normal state resistivity.

The time derivative of the temperature field is given by Newton's law of cooling:

$$c\dot{T}(x,y) = \kappa\nabla^2 T(x,y) - h(T(x,y) - T_0)/d + \mathbf{J}\cdot\mathbf{E}/d \tag{3.16}$$

Here c is the specific heat of the superconductor. The first term on the right represents thermal diffusion in the plane of the film, with κ being the in plane heat conductivity. The second term is Newtons law of cooling. We have assumed that the substrate has constant temperature T_0. Thus the heat transfer to the substrate is characterized by the coefficient h. The last term, $\mathbf{J}\cdot\mathbf{E}/d$, is the Joule heating. Because the electric field is parallel to the current field, we can simplify Equation 3.16:

$$\dot{T} = \frac{\kappa}{c}\nabla^2 T - h(T(x,y) - T_0)/cd + JE/cd \tag{3.17}$$

We see that the evolution of temperature depends on the thickness d of the film. This means that reduction of thickness, like in Section 2.1, would result in additional effects; not just a reduction of the critical current. However these effects are only important for flux avalanches. The dendritic avalanches are triggered by a heat pulse; the temperature is artificially raised to $1.5\,T_c$ for a short time. The pulse is typically placed on the edge of the sample, because this is where dendritic avalanches start in experiments.

The time scale for flux avalanches is much smaller that the time scale used in stable simulations. We need a timescale which makes $\left|\frac{d\tilde{H}_a}{d\tilde{t}}\right| \ll 1$. In [16] the time scale is the decay time of currents in normal material:

$$\tilde{t} = t\rho_0/dw_0. \tag{3.18}$$

Here ρ_0 is the resistivity of the material when $T = T_c$. For temperature $\tilde{T} = T/T_c$ is a natural choice. The sheet current J is scaled to the critical sheet current at absolute zero temperature:

$$\tilde{J} = J/(dj_{c0}),$$

where j_{c0} is the critical current density at $T = 0$. Because $E = \rho j$ we scale E using the same quantities used to scale resistivity and current:

$$\tilde{E} = E/\rho_0 j_{c0} \tag{3.19}$$

Using the dimensionalless quantities defined above, we can write Equation 3.17 on dimensionalless form:

$$\begin{aligned}
\dot{T} &= \frac{\kappa}{c}\nabla^2 T - h(T(x,y) - T_0)/cd + JE/cd \\
\frac{T_c}{(\rho_0/dw\mu_0)^{-1}}\frac{\partial \tilde{T}}{\partial \tilde{t}} &= \frac{\kappa}{c}\nabla^2 T_c\tilde{T} - h(T_c\tilde{T} - T_c\tilde{T}_0)/cd + (dj_{c0})\tilde{J}\rho_0 j_{c0}\tilde{E}/cd \\
\frac{\partial \tilde{T}}{\partial \tilde{t}} &= (d\omega\mu_0/\rho_0)\frac{\kappa}{c}\nabla^2\tilde{T} - (d\omega\mu_0/\rho_0)h(\tilde{T} - \tilde{T}_0)/cd \\
&\quad + (d\omega\mu_0/\rho_0 T_c)(dj_{c0})\tilde{J}\rho_0 j_{c0}\tilde{E}/(cd) \\
\frac{\partial \tilde{T}}{\partial \tilde{t}} &= (d\omega\mu_0\kappa/\rho_0 c)\nabla^2\tilde{T} - (d\omega\mu_0 h/\rho_0 cd)(\tilde{T} - \tilde{T}_0) + (dj_{c0}^2\omega\mu_0/cT_c)\tilde{J}\tilde{E}
\end{aligned} \tag{3.20}$$

This equation can be rewritten as

$$\begin{aligned}
&\frac{\partial \tilde{T}}{\partial \tilde{t}} = \alpha\nabla^2\tilde{T} - \beta(\tilde{T} - \tilde{T}_0) + \gamma\overline{\gamma}\tilde{J}\tilde{E} \\
&\alpha \equiv \frac{d\omega\mu_0\kappa}{\rho_0 c}\,, \quad \beta \equiv \frac{d\omega\mu_0 h}{\rho_0 cd}\,, \quad \gamma \equiv (\mu_0\omega d j_{c0}^2\omega/cT_c)\,, \quad \overline{\gamma}(T) \equiv c(T_c)/c(T)
\end{aligned} \tag{3.21}$$

Here $\overline{\gamma}(T) = \tilde{T}^{-3}$ represents a temperature dependence from the parameters which does not cancel out.

In the simulation program the discrete time derivative of the temperature is implemented as

$$\frac{\partial \tilde{T}}{\partial \tilde{t}} \to (T_{n+1} - T_n)/\Delta t_n. \tag{3.22}$$

Δt_n is the variable time step at time step number n. Also

$$T \to (T_{n+1} + T_n)/2. \tag{3.23}$$

The task at hand is to find the expression for T_{n+1}. However the ∇^2 operator in inconvenient to work with. Therefore we will solve the equation in Fourier-space. We use the following notation for the Fourier transformation of temperature:

$$\mathcal{F}[T_i] = T^{(i)} \tag{3.24}$$

Using this notation we get

$$\mathcal{F}\left[\frac{\partial \tilde{T}}{\partial \tilde{t}}\right] \to (T^{(n+1)} - T^{(n)})/\Delta t_n \ , \quad \mathcal{F}[T] \to (T^{(n+1)} + T^{(n)})/2$$

The Fourier transform of 3.21 becomes:

$$\mathcal{F}\left[\frac{\partial \tilde{T}}{\partial \tilde{t}}\right] = \alpha(ik)^2\mathcal{F}[\tilde{T}] - \beta(\mathcal{F}[\tilde{T}] - \mathcal{F}[\tilde{T}_0]) + \mathcal{F}[\gamma\overline{\gamma}\tilde{J}\tilde{E}] \tag{3.25}$$

Using the substitutions from Equatnion 3.22 and Equation 3.23 we get:

$$(T^{(n+1)} - T^{(n)})/\Delta t_n = \alpha(ik)^2(T^{(n+1)} + T^{(n)})/2 - \beta\left((T^{(n+1)} + T^{(n)})/2 - \mathcal{F}[\tilde{T}_0]\right) + \mathcal{F}[\gamma\overline{\gamma}\tilde{J}\tilde{E}]$$

$$\left(1/\Delta t_n + \alpha k^2/2 + \beta/2\right) T^{(n+1)} = \left(1/\Delta t_n - \alpha k^2/2 - \beta/2\right) T^{(n)} + \beta\mathcal{F}[\tilde{T}_0] + \mathcal{F}[\gamma\overline{\gamma}\tilde{J}\tilde{E}]$$

Multiplying by Δt_n and simplifying:

$$\left(1 + (\alpha k^2 + \beta)\Delta t_n/2\right) T^{(n+1)} = \left(1 - (\alpha k^2 + \beta)\Delta t_n/2\right) T^{(n)} + \left(\beta\mathcal{F}[\tilde{T}_0] + \mathcal{F}[\gamma\overline{\gamma}\tilde{J}\tilde{E}]\right) \Delta t_n$$

Our solution for the next time step t_{n+1} then becomes

$$T^{(n+1)} = \frac{1 - (\alpha k^2 + \beta)\Delta t_n/2}{1 + (\alpha k^2 + \beta)\Delta t_n/2} T^{(n)} + \frac{\mathcal{F}[\beta\tilde{T}_0 + \gamma\overline{\gamma}\tilde{J}\tilde{E}]}{1 + (\alpha k^2 + \beta)\Delta t_n/2} \Delta t_n \tag{3.26}$$

In the simulations in this thesis we will use

$$T_0 = 0.4\,T_c, \ \alpha = 10^{-6}, \ \beta = 0.03, \ \gamma = 15.0 \tag{3.27}$$

Chapter 4

Results and Discussion

In Chapter 2 we discussed how macroscopic anisotropy can be manufactured by lowering the critical sheet current J_c in channels with constant width and constant spacing. In Section 3.2 we outlined the numerical methods used for finding the evolution of the screening currents and magnetic self field given a ramping protocol, including simulations of flux avalanches. In this chapter we apply the simulation program to samples with manufactured anisotropy.

4.1 Width of channels equal to spacing

The simplest case of channel pattern is when the spacing between the channels is equal to the width of the channel. This means that $b = c$ and the period of the alternating pattern is $b + c = 2b$. For the simulations we have to specify both the critical current in these channels and their width. In order to study the effect that the width has on the magnetic flux distribution, we do simulations on a selection of widths: $b = 4, 6, 16, 32$ and 64 grid points. We use the same sample resolution in each simulation: 732x732 grid points. The system is 1024x1024 grid points if we include the vacuum that surrounds the samples. We understand that a channel width of 64 grid points is quite large for such a sample. It is however important to study the extreme cases in order to get a fuller understanding of the phenomena. The other extreme case is when the width is 4 grid points. In this case our perturbations are dangerously close to the grid resolution. While simulation results should always be interpreted with skepticism, phenomena on pixel level is even less trustworthy.

For the channels we have chosen the critical sheet current to be $J_{c1} = 3/4$ relative to J_c outside the channels, which is still normalized to unity.

In Figure 4.1 we have listed the resulting magnetic distributions. For the sample with the widest channels we have included the corresponding matrix for critical current in Figure 4.1(f). This makes it possible to see how the underlying critical current alters the penetration pattern of the magnetic field. We see that in the channels of $J_c = 3/4 = 0.75$,

the black regions in Figure 4.1(f), the magnetic field is much more uniform and has a higher value. The regions of higher critical sheet current are darker, which results in a pattern of dark stripes in the north and south trapezoid shaped regions.

The pattern of dark stripes is visible for all channel widths, but it becomes faint for $b = c = 4$ (Figure 4.1(a)) and $b = c = 6$ (Figure 4.1(b)). Except for the anisotropy, the flux penetration is similar to that of a sample with uniform J_c, like in Figure 1.6(a). The simulations for $b = c = 4$ and $b = c = 6$ have thus achieved a flux penetration that is both smooth and anisotropic.

In our case $b = c$ which means that we can use Equation 2.9 to find a theoretical estimate for the anisotropy factor:

$$a = (1/J_{c1} + 1)/2 = (1/(3/4) + 1)/2 = 7/6 \tag{4.1}$$

Remember that the formula assumes a Bean model where there is no flux creep, which means $n \to \infty$. The derivation also ignores any effects caused by fine structure in the current. By this we mean the current kinks drawn in Figure 2.3. The anisotropy factor corresponds to the inclination of the D-lines. A large value of a corresponds to high anisotropy. This means that the D-lines will meet farther away form the center than for smaller a. In Figure 4.2 we have zoomed in on the north-west D-line in each sample in Figure 4.1. This way it is easier to see the details of the penetration pattern. For each sub-figure 4.2(a) - 4.2(e) we have plotted two dashed lines starting from the north-west corners, one white and one black. The black one represents the D-line corresponding to the anisotropy factor $a = 7/6$ from the calculations above. Interestingly this line does not agree with the actual D-lines. The white line is a guide for the eye for where the D-lines lie, making it easier to see the error in our estimate for the anisotropy factor. The anisotropy factors corresponding to the white lines are recorded in Table 4.1. It must be said that for $b = 32$ pixels and $b = 64$ pixels we do not have well defined D-lines as they are far from straight. Thus the anisotropy factor is not an appropriate quantity for these states.

For $b = c = 4$ grid points we have a particularly small anisotropy factor. The general tendency is that the anisotropy factors in the simulations are smaller than the one predicted by Equation 4.1. The simulation results in Figure 4.1(b), show a higher anisotropy factor compared to 4.1(a). Also the flux penetration is quite smooth compared to the results in Figures 4.1(c)-4.1(e). Therefore $b = c$ is the most promising choice of widths.

Table 4.1: The anisotropy factor for each simulation shown in Figure 4.2.

b [pixels]	4	6	16	32	64
c [pixels]	4	6	16	32	64
a [dimensionalless]	1.035	1.08	1.08	1.09	1.08

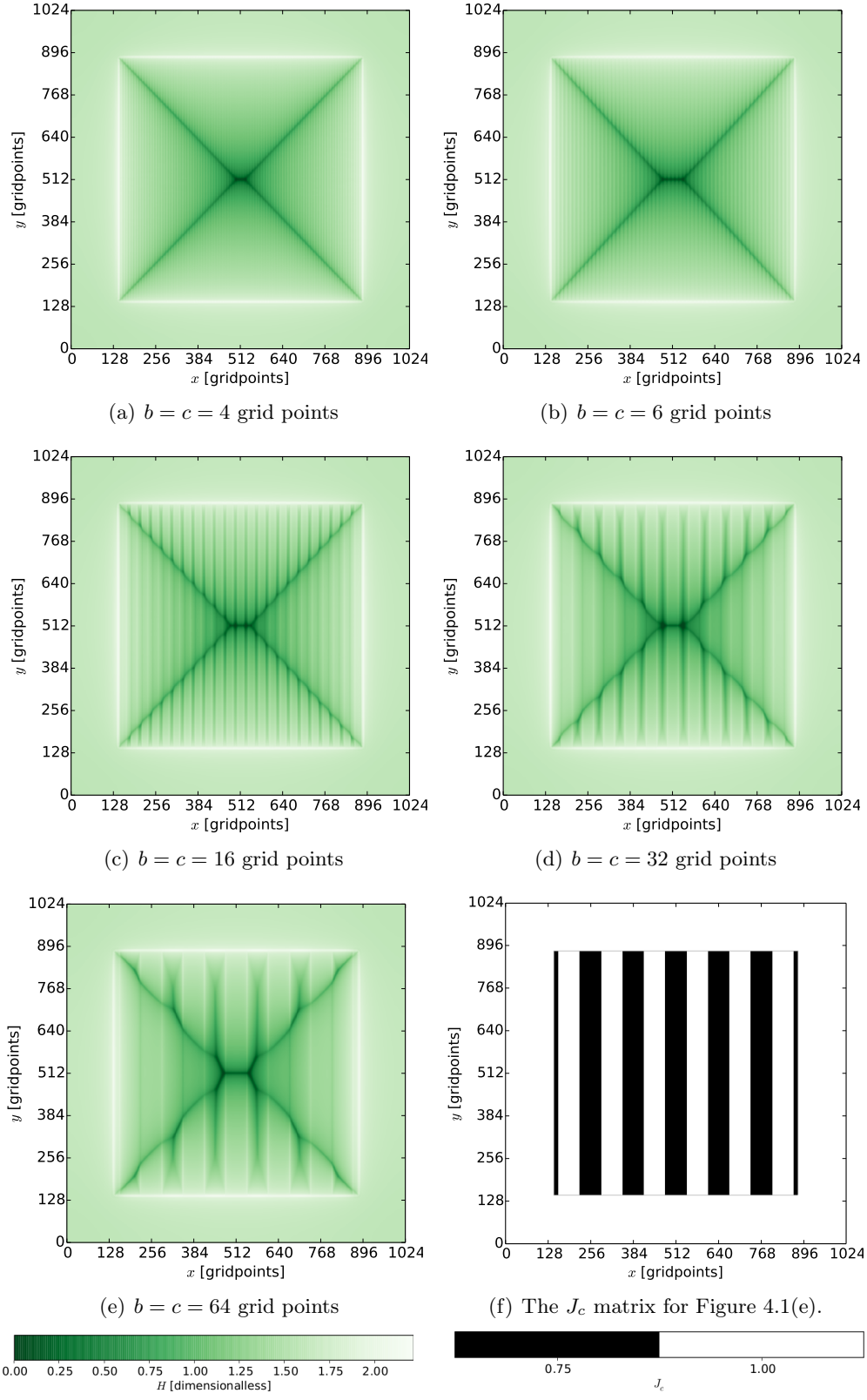

(a) $b = c = 4$ grid points

(b) $b = c = 6$ grid points

(c) $b = c = 16$ grid points

(d) $b = c = 32$ grid points

(e) $b = c = 64$ grid points

(f) The J_c matrix for Figure 4.1(e).

Figure 4.1: Varying the period of the channel patterns.

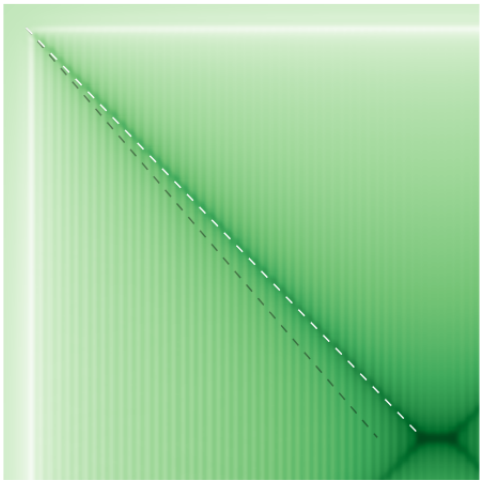

(a) $b = c = 4$ grid points

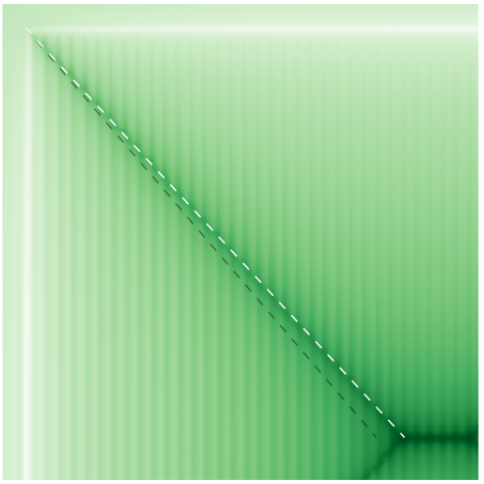

(b) $b = c = 6$ grid points

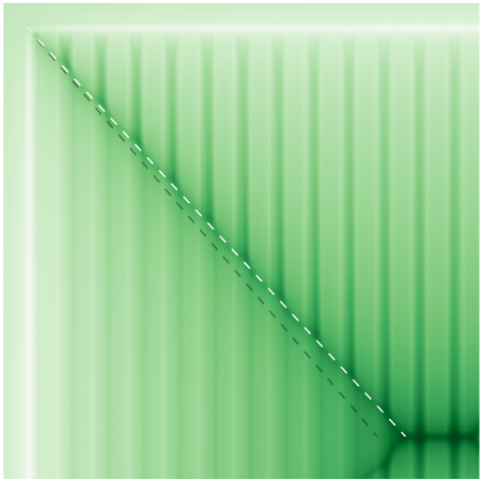

(c) $b = c = 16$ grid points

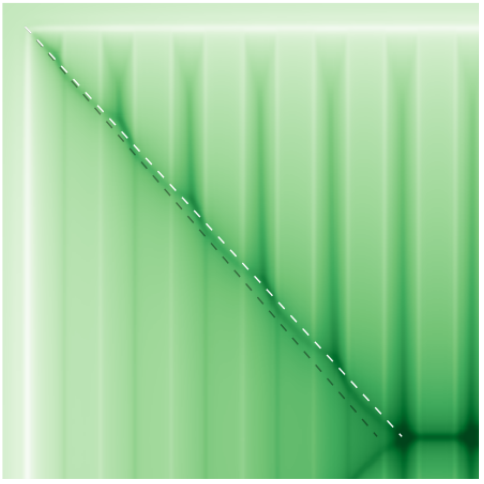

(d) $b = c = 32$ grid points

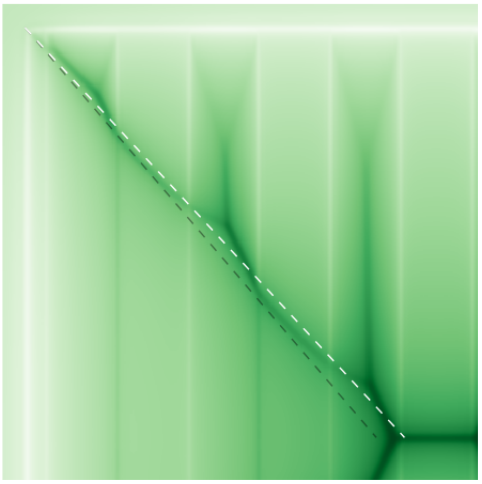

(e) $b = c = 64$ grid points

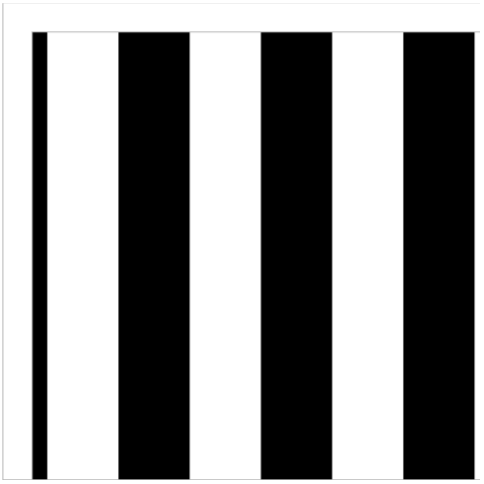

(f) The J_c matrix corresponding to Figure 4.2(e). See 4.1(f) for colorbar.

Figure 4.2: Close ups of Figures 4.1(a)-4.1(f). The dashed black lines correspond to our theoretical calculation of the anisotropy factor. The dashed white lines approximate the D-lines we actually see.

4.1.1 Study of the distribution of magnetic field

Figure 4.1(e) is well suited for studying the magnetic field distribution resulting from the channel perturbations of J_c. Figure 4.3(a) shows the same magnetic field distribution as in Figure 4.2(e), but four regions have been marked in gray and numbered from 1 to 4. Each region shows a distinct qualitative behavior in the flux distribution, which is repeated periodically in the horizontal direction. Regions of type 1 and 2 alternate in the north and south part of the sample. Regions of type 3 and 4 alternate in the west and east part. Regions of type 1 and 3 correspond to reduced critical sheet current. In Figure 4.3(a) we cannot see the eastern and southern parts of the sample, but because of the symmetry of Figure 4.1(e), the behavior in the northern part is equivalent to the southern part and the western part equivalent to the eastern part.

Region 2 shows the same type of flux distribution that is largely similar to what is seen in rectangular freestanding samples, like Figure 1.6(a). From each top corner of region 2 we can see a faint dark D-line. These D-lines join and continue south, forming the letter "Y". These D-lines indicate sharp turns in the current streamlines, just like we have at the D-lines in a rectangular sample. We can see more regions with this behavior and we call these *regions of type 2*. In between regions of type 2 we have regions of *type 1*, where the critical current is lower. Therefore the magnetic field is not screened as effectively in regions of type 1 and therefore they appear brighter than regions of type 2 in Figure 4.2(e). For samples with a very tight stripe pattern, like Figure 4.1(a) and 4.1(b), the regions of type 1 and type 2 become very thin. Therefore it is hard to study the flux distribution in detail. For these samples the penetration pattern looks like the teeth of a comb, entering from the sample's top and bottom edges.

Let us return to the Flux distribution of Figure 4.3(a). In region 3 and 4 we see a different situation to the one in type 1 and type 2 regions. The flux penetration in region 3 and region 4 is quite uniform, except for alternating dark and bright stripes in between them. The critical sheet current in region 3 is 3/4 relative to J_c in region 4. As seen in Figure 4.3(b) the current is almost parallel to the channels. Figure 4.5(a) shows that the current along the channels reaches approximately $J_y = 0.75$ in region 3 and $J_y = 1$ in region 4. At least measured along a horizontal line going through the middle of the sample, $y = 512$ [grid points]. Flux creep appears to be the reason that the current doesn't fully reach the critical sheet current, just like we see in Figure 1.6(e).

If there was no flux creep, we would expect the streamlines to be similar to those shown in Figure 4.4. These streamlines are the output from the computer program in Appendix A and the algorithm was discussed in Section 3.1. In Figure 4.4 we see that the streamlines in the Bean model are much more angular than the streamlines in Figure 4.3(b). They also resemble the idealized streamlines shown in Figure 2.3, which are valid for zero flux creep. Flux creep is therefore the most likely reason for the low observed

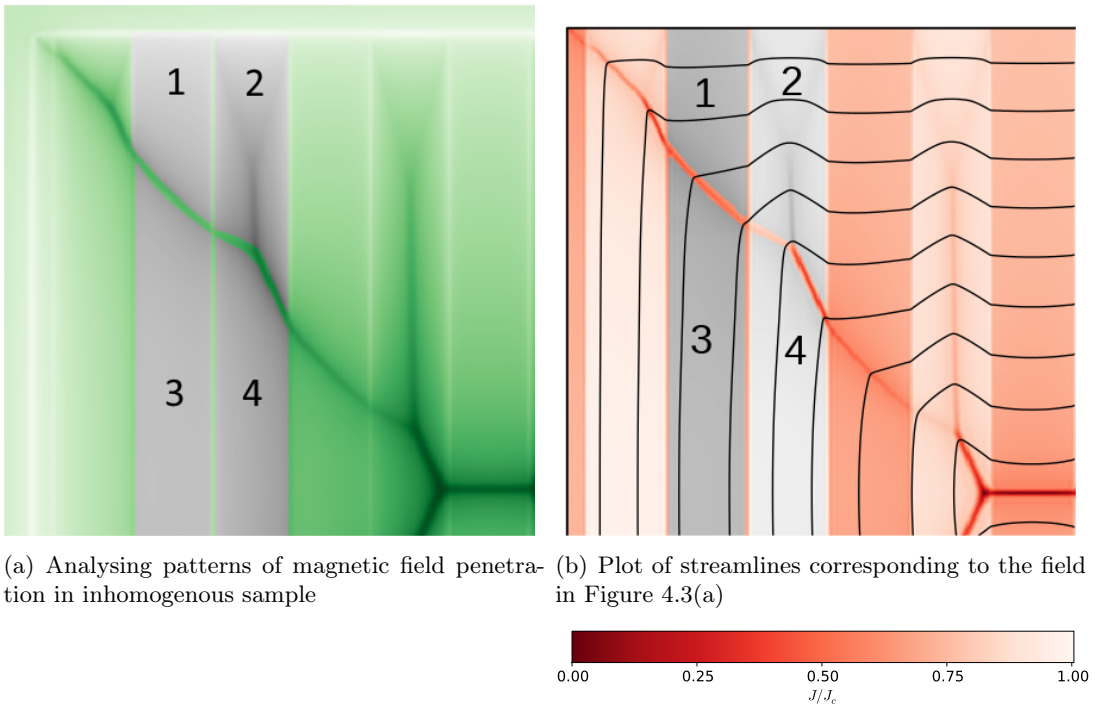

(a) Analysing patterns of magnetic field penetration in inhomogenous sample

(b) Plot of streamlines corresponding to the field in Figure 4.3(a)

Figure 4.3: Analysis of regions where the magnetic- and current-field has distinct behavior.

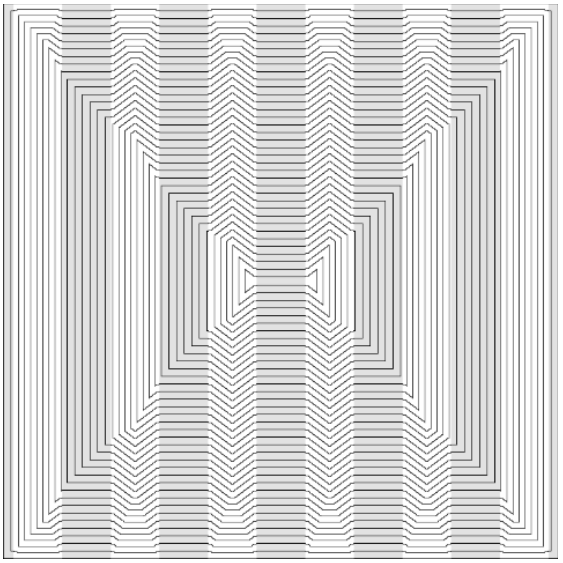

Figure 4.4: The streamlines calculated using Bean model assumptions for the J_c matrix shown in Figure 4.1(f). At full magnetic field penetration. The critical current in the gray areas is 75% of the critical current in the white areas.

value for the anisotropy factor in table 4.1. We study this effect more closely in Section 4.3

Let us return to Figure 4.3(b). Just as in Figure 4.3(a), we have marked the numbered regions in gray. The curvature of the streamlines determine how effective the current is at screening the applied magnetic field. Inside region 2 the streamlines curve in the

direction of internal screening of magnetic field. This makes regions of type 2 darker in Figure 4.3(a) compared to regions of type 1. The same happens on the D-lines inside region 2 in Figure 4.3(a). These small D-lines correspond to the current kinks on the dashed lines in Figure 2.3. The current kinks are better defined in the Bean state in Figure 4.4 and therefore easier to see than in Figure 4.3(b). Thus Figure 4.4 makes it easier to do a qualitative study. On the western and eastern border of region 2, the streamlines curve the opposite direction of the screening direction. This increases the magnetic field locally along the borders between type 1 and 2 regions. This is seen in Figure 4.3(a) as bright vertical stripes.

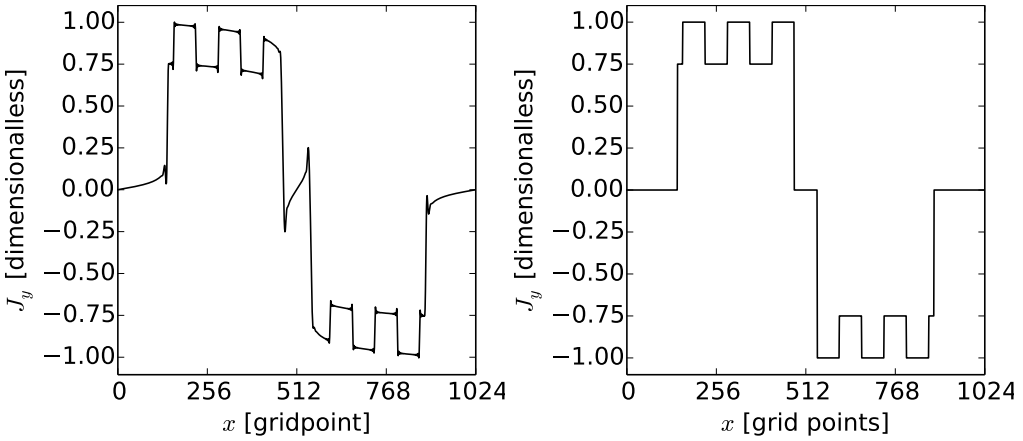

(a) J_y profile along $y = 512$ of the simulation corresponding to 4.1(e).

(b) Simlified version of the current profile in Figure 4.5(a).

Figure 4.5: Current profiles

We will now study the alternating black and white stripes between regions of type 1 and type 2, seen in Figure 4.2(e). In the transition between high and low screening current there are lines of strong(bright) and weak(dark) magnetic field. The current profile of J_y, measured across the channels, through the middle of the sample, is has been plotted in Figure 4.5(a). In order to simplify our study, we ignore the details in the current profile and introduce an artificial current profile in Figure 4.5(b). Here J_y reaches the local critical sheet current, except for in the middle of the sample and outside the sample. From this artificial current profile we have created a 2 dimensional current distribution which has been plotted in Figure 4.6(a). The current is assumed to reach the local value of J_c and be parallel to the y-axis. Therefore the current is either 0, ± 0.75 or ± 1 of J_c, where the sign gives the direction along the y-axis. This current field does neglect the current that should be flowing in the northern and southern trapezoids of the sample. Of course this does not represent a physical system[1] as it does not fulfill continuity of current. However, it does provide a simple current field which will yield a

[1]The simplification done here may be unsatisfactory to many. However, in physics we have to make an intelligent choice in what effects we may neglect in order to study the impact of other more dominant effects.

magnetic self field which will be easy to interpret. Our purpose is to calculate the self field from the alternating high ($J = 1$ [dimensionalless] in regions of type 4) and low ($J = 0.75$ [dimensionalless] in regions of type 3) screening currents that seem to cause the bright and dark lines in Figure 4.1(e). The neglected parts of the current field is far away from the regions of interest and will have minor impact on the self field in regions of type 1 and type 2. Biot-Savart's law tells us how to calculate the magnetic self field

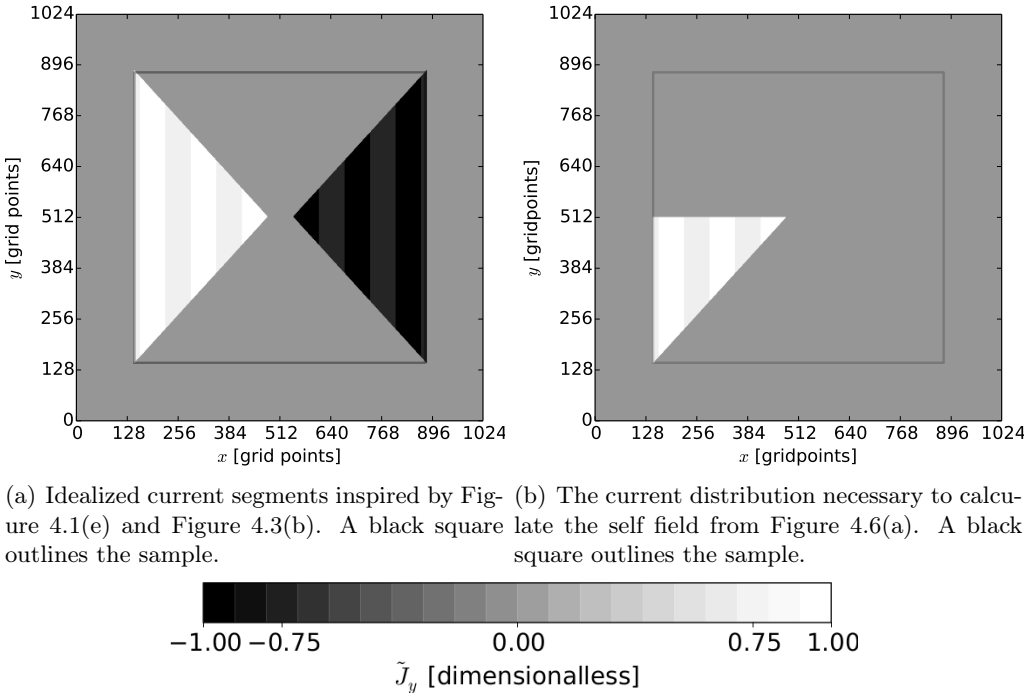

(a) Idealized current segments inspired by Figure 4.1(e) and Figure 4.3(b). A black square outlines the sample.

(b) The current distribution necessary to calculate the self field from Figure 4.6(a). A black square outlines the sample.

Figure 4.6: Current distribution used to calculate self field.

from the current field in Figure 4.6(a). The magnetic field $\mathbf{B}$ at a point $\mathbf{r}$ is

$$\mathbf{B}(\mathbf{r}) = \frac{\mu_0}{4\pi} \int\int\int_V \frac{\mathbf{j}(\mathbf{r}') \times (\mathbf{r}' - \mathbf{r})}{|\mathbf{r}' - \mathbf{r}|^3} dV. \tag{4.2}$$

Here μ_0 is the permeability of vacuum, $\mathbf{j}(\mathbf{r}')$ is the current density at a point $\mathbf{r}'$. The integration is over all space in all three dimensions. μ_0 can be removed from our expression by changing to magnetic field strength:

$$\mathbf{H}(\mathbf{r}) = \frac{1}{4\pi} \int\int\int_V \frac{\mathbf{j} \times (\mathbf{r}' - \mathbf{r})}{|\mathbf{r}' - \mathbf{r}|^3} dV = \frac{1}{4\pi} \int_{-\infty}^{\infty}\int_{-\infty}^{\infty}\int_{-\infty}^{\infty} \frac{\mathbf{J}(x', y', z')\delta(z') \times (\mathbf{r}' - \mathbf{r})}{|\mathbf{r}' - \mathbf{r}|^3} dz' dy' dx'$$

$$= \frac{1}{4\pi} \int_{-\infty}^{\infty}\int_{-\infty}^{\infty} \frac{\mathbf{J}(x, y, z = 0) \times (\mathbf{r}' - \mathbf{r})}{|\mathbf{r}' - \mathbf{r}|^3} dy' dx' \tag{4.3}$$

We see that the term

$$\frac{(\mathbf{r}' - \mathbf{r})}{|\mathbf{r}' - \mathbf{r}|^3} dy' dx'$$

is dimensionalless. Thus the magnetic field strength has the same units as the sheet current density: A/m. We can divide the expression for $\mathbf{H}(\mathbf{r})$ by the maximum critical sheet current $J_{c,0}$ to obtain Equation 4.3 on dimensionalless form:

$$\begin{aligned} \tilde{\mathbf{H}}(\mathbf{r}) = \mathbf{H}(\mathbf{r})/J_{c0} &= \frac{1}{4\pi J_{c0}} \int_{-\infty}^{\infty} \int_{-\infty}^{\infty} \frac{\mathbf{J}(x', y', z' = 0) \times (\mathbf{r}' - \mathbf{r})}{(\mathbf{r}' - \mathbf{r})^3} dy' dx' \\ &= \frac{1}{4\pi} \int_{-\infty}^{\infty} \int_{-\infty}^{\infty} \frac{\tilde{\mathbf{J}}(x, y, z = 0) \times (\mathbf{r}' - \mathbf{r})}{|\mathbf{r}' - \mathbf{r}|^3} dy' dx', \end{aligned} \tag{4.4}$$

where $\tilde{\mathbf{J}} \equiv \mathbf{J}/J_{c0}$.

It is a trivial task to calculate the field numerically by replacing the integral by a finite sum:

$$\tilde{\mathbf{H}}(x, y) = \frac{1}{4\pi} \sum_{n=0}^{N} \sum_{m=0}^{M} \frac{\tilde{\mathbf{J}}(x'_n, y'_m) \times ((x'_n - x)\hat{\mathbf{i}} + (y'_m - y)\hat{\mathbf{j}})}{((x'_n - x)^2 + (y'_m - y)^2)^{3/2}} a^2 \tag{4.5}$$

Here we have replaced $dx'dy'$ by a^2 which is the area of a current element in the sample. x'_n and y'_n are defined as

$$x'_n = na\,, \quad y'_n = ma$$

and the dimensions of the sample is

$$L_x = Na\,, \quad L_y = Ma$$

The cross product in Equation 4.5 can be simplified because $\tilde{\mathbf{J}} \perp \hat{\mathbf{i}}$:

$$\tilde{\mathbf{H}}(x, y) = \frac{a^2}{4\pi} \sum_{n=0}^{N} \sum_{m=0}^{M} \frac{-\tilde{J}(x'_n, y'_m)(x'_n - x)\hat{\mathbf{k}}}{((x'_n - x)^2 + (y'_m - y)^2)^{3/2}} \tag{4.6}$$

We choose $M = 1023$ and $N = 1023$, which corresponds to a 1024×1024 sample like in Figure 4.1(e). For simplicity we choose $a = 1$. The current distribution is shown in Figure 4.6(a)

When programming this calculation we see that the symmetry in the current distribution will let us get away with calculating only $1/4$ of the calculations in 4.6. We can calculate the magnetic field produced by the current distribution in Figure 4.6(b) and then rotate the resulting matrix to find the solution from the rest of the current distribution in Figure 4.6(a). The program code is provided in Appendix B. The Resulting self field is shown in Figure 4.7. We can see a striking similarity to the alternating vertical lines of low and high magnetic flux we see in Figure 4.1(e).

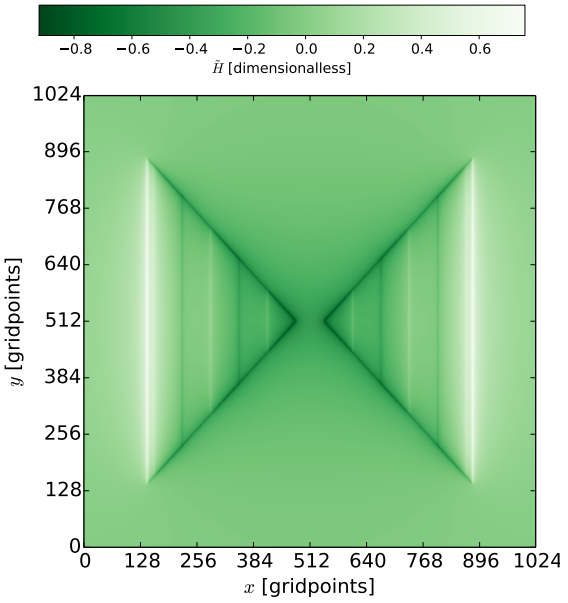

Figure 4.7: Self field resulting from calculations.

4.2 Systematic variation of the reduction of critical sheet current in the channels

We have studied the effect of the width of channels in samples where the channels have the same width as the distance in between them. We can also vary how much the critical current is reduced in the channels. For this section we run simulations for $b = c = 6$ grid points and

$$J_{c1} = 0.7,\ 0.75,\ 0.8,\ 0.85$$

in the channels. $J_{c1} = 0.7$, $b = c = 6$ has already been simulated in Section 4.1. As $b = c$, we know that

$$a = (1/J_{c1} + 1)/2. \tag{4.7}$$

The expected anisotropy factors, for samples with no flux creep, are listed in Table 4.2.

Table 4.2: The anisotropy factor predicted for each value of J_{c1}/J_{c0}, assuming no flux creep.

J_{c1}/J_{c0}	0.7	0.75	0.8	0.85
a [dimensionalless]	1.21	1.17	1.125	1.09

In Figure 4.8 we have plotted the flux distributions resulting from ramping each sample to full magnetic field penetration. As for the simulations in Section 4.2, we see that our theoretical model for anisotropy over estimates the anisotropy factor. The actual anisotropy factors are listed in Table 4.3.

The actual anisotropy factor for $J_{c1}/J_{c0} = 0.70$ (Figure 4.8(a)) is quite large. Unfortunately these larger reductions of J_c result in slow computation speed because the

Table 4.3: The actual anisotropy factor a measured in the simulation results in Figure 4.8.

J_{c1}/J_{c0}	0.7	0.75	0.8	0.85
a [dimensionalless]	1.12	1.08	1.07	1.045

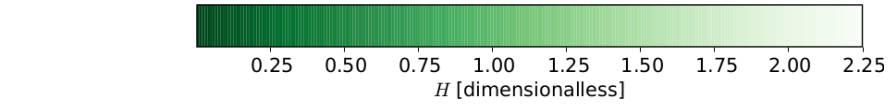

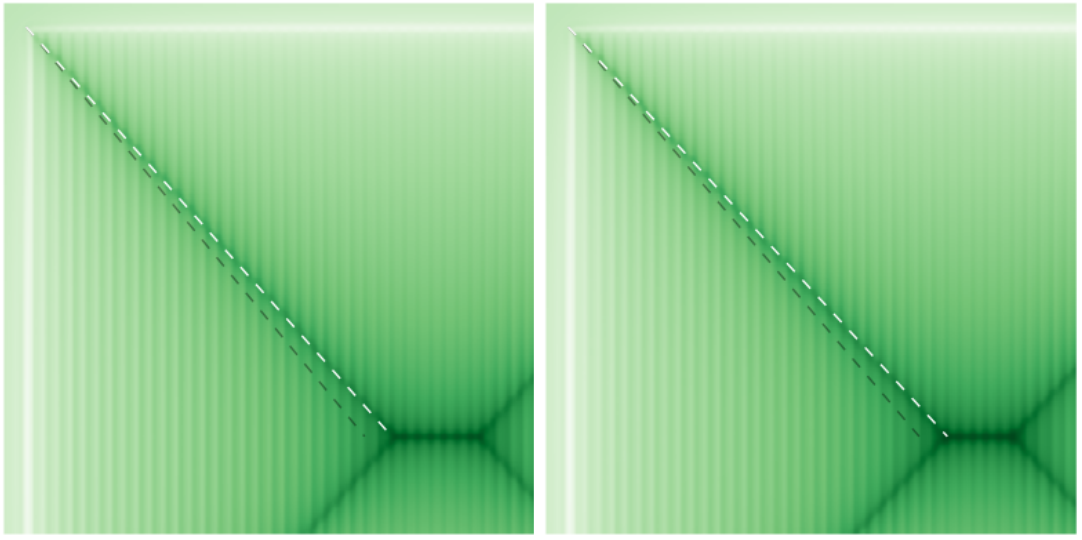

(a) $J_{c1}/J_{c0} = 0.70$ (b) $J_{c1}/J_{c0} = 0.75$

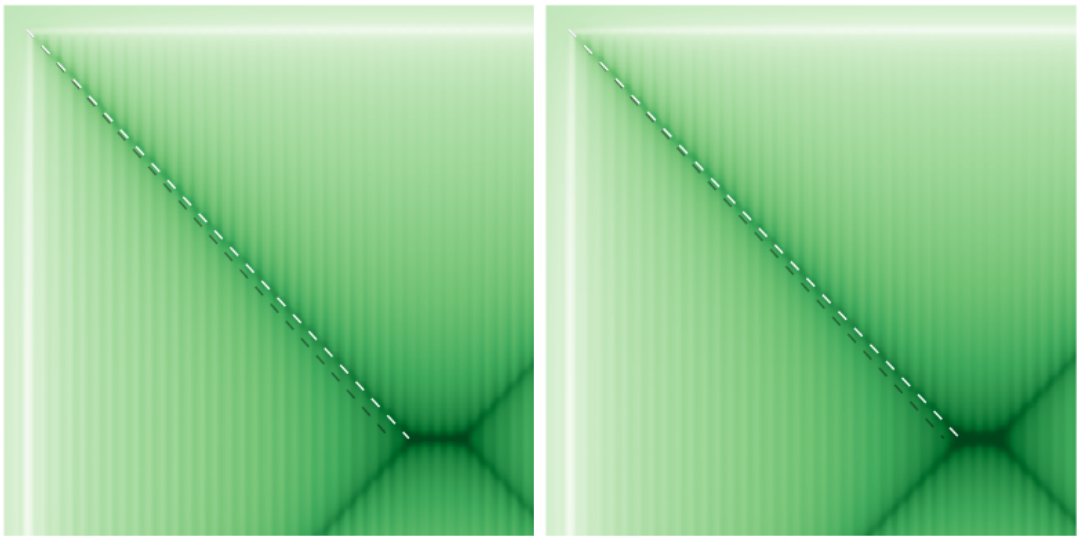

(c) $J_{c1}/J_{c0} = 0.80$ (d) $J_{c1}/J_{c0} = 0.85$

Figure 4.8: At full field penetration for $b = c = 6$ for different values of p.

discontinuous step is very large. For $J_{c1}/J_{c0} = 0.70$ (Figure 4.8(a)) we see a slightly more moderate anisotropy. For further studies we will use $b = c = 6$ and $J_{c1}/J_{c0} = 0.75$ as this combination has shown a good compromise between smoothness in its field distribution, relatively large anisotropy and stability in calculations. For the higher values of J_{c1}/J_{c0}

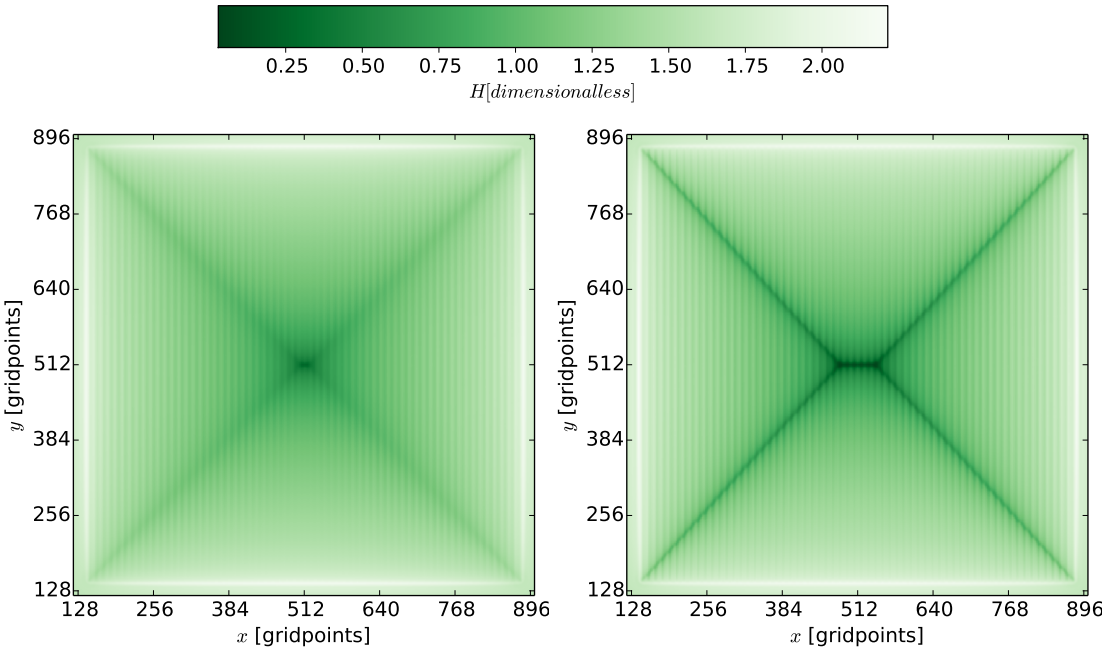

(a) $n = 5$ (b) $n = 19$

Figure 4.9: How flux creep destroys anisotropy. $b = c = 6$

we get less anisotropy, as expected. For $J_{c1}/J_{c0} = 0.85$ the anisotropy almost disappears.

4.3 The importance of flux creep

Until now we have only used $n = 19$ as the creep exponent, which is considered a moderate value. Increasing the value of n will decrease the flux creep and thus bring our results closer to the Bean model. However, it will also increase the nonlinearity of the material law in Equation 1.45. Simulations for $b = c = 6$, $J_{c1}/J_{c0} = 0.75$, $n = 29$ yielded too much numerical error and ran slowly. Instead we choose $n = 5$, keeping the other parameters equal. The resulting magnetic field distribution is plotted in Figure 4.9(a). For the purpose of comparison we have also included the results for $n = 19$ in Figure 4.9(b), which is equivalent to Figure 4.1(b). We see that for $n = 5$ we have almost no appreciable anisotropy as the D-lines meet extremely close to the center of the sample.

In Figure 4.10(a) we see that for $n = 5$ the streamlines are much more rounded off in the corners compared to the streamlines for $n = 19$ which is shown in Figure 4.10(b) simulation for $n = 19$. This is the reason that the D-lines are very weak in Figure 4.9(a). Figure 4.11 shows the current profile of $J_y(x, y = 512)$. This is the current component flowing parallel to the channels and $y = 512$ corresponds to the middle of the samples. We see that the current is smeared out much more for $n = 5$ than for $n = 19$. Neither of the current profiles reach the critical sheet current perfectly. However, for $n = 19$ the current does not decay as quickly from the sample edge and reaches much closer to

the local J_c. We see that the creep of current is much higher for $n = 5$ as much of the current ends up in the middle of the sample. For high values of n we get closer to the current assumed by our estimate from Section 2.2.2. Thus we need a high value for n if we want to construct macroscopic anisotropy. Because $n \propto 1/T$, high n corresponds to low temperature. For higher values of n we increase the non-linearity of the resistivity in Equation 1.34. This leads to increased numerical instability and therefore our simulations for significantly higher n ($n = 29$ and $n = 39$) were not successful.

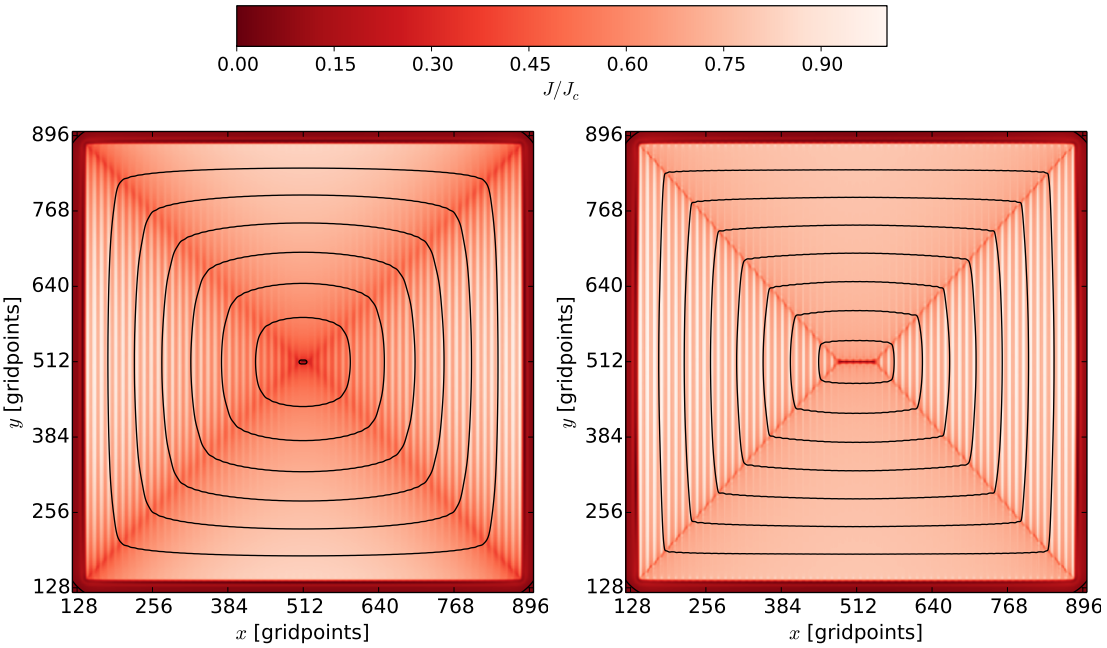

(a) $n = 5$ (b) $n = 19$

Figure 4.10: The current distributions and current streamlines for simulations where $n = 5$ and $n = 19$.

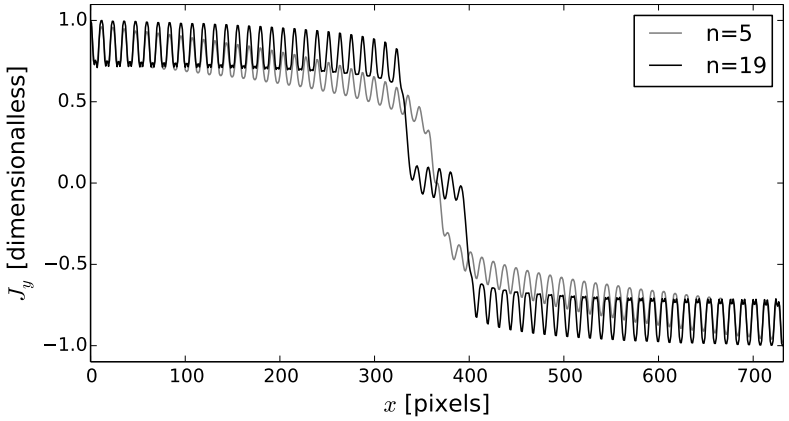

Figure 4.11: Comparison of current profiles for $n = 5$ and $n = 19$.

4.4 Dendrites in sample with channels

In this section we will compare dendritic flux avalanches in uniform samples to avalanches in samples with a periodic pattern of channels. For the uniform sample we have chosen a system resolution (including vacuum) of 1024×1024, where the sample is centered in the middle and occupies $5/7$ of the system. As before we use samples with $n = 19$ and we have chosen $b = c = 6$ grid points. The samples are prepared for dendrite nucleation by ramping the applied magnetic field H_a to a small value. We have used $\tilde{H}_a = 0.2$ (dimensional less) before nucleation. Remember that in Section 1.10 we ramped up to $\tilde{H}_a = 1.5$ to reach full field penetration of the sample.

We will compare the dendrites in a sample of uniform J_c to the dendrites in the sample with channels where $J_{c1} = 3/4 J_{c0}$. For the uniform sample we nucleate one dendrite on the middle of the edge and one off center. The resulting dendrites are shown in Figure 4.12(a) and 4.12(b). The dendrite which was triggered on the center of the edge behaves quite symmetrically, Figure 4.12(a). Even though the branching is random, we see that they are similar in length and direction on each side of $y = 512$. The dendrite which is triggered off center tends to branch towards the diagonal of the sample. Both of these dendrites show traditional behavior.

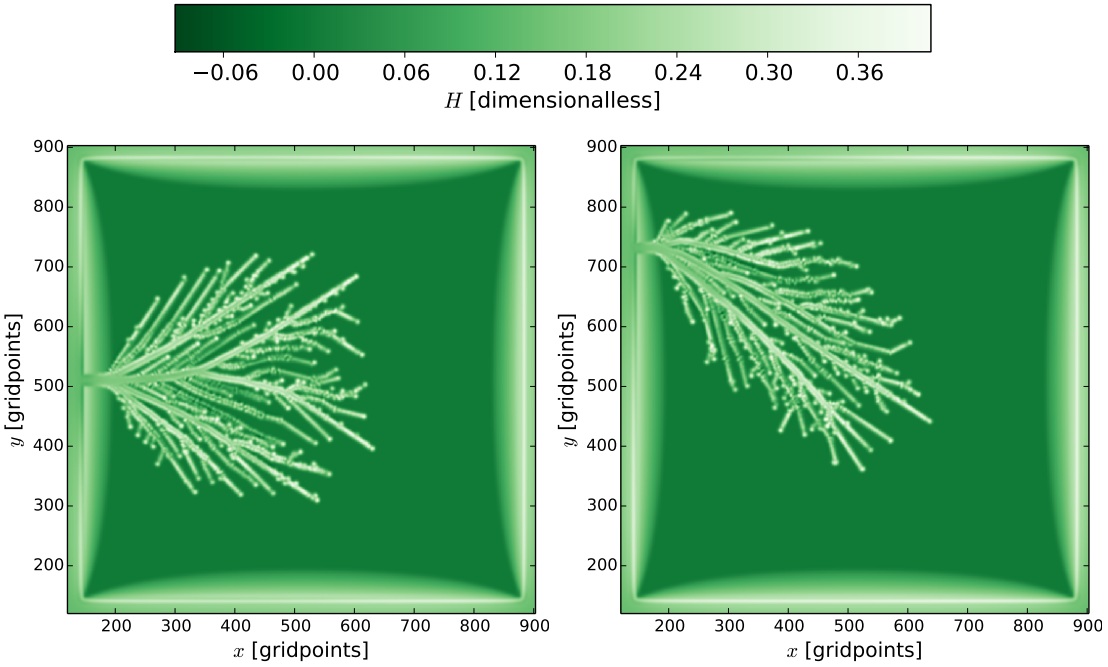

(a) Dendrite triggered on the center of the edge

(b) Dendrite triggered off center

Figure 4.12: Simulation results for dendritic avalanches in uniform samples.

For the samples with channels we trigger the dendrites at the same places as we did for the uniform samples. However, because of the channels, we can rotate the sample by 90 degrees which results in a different situation. In Figure 4.13 we trigger the dendrites

so that their initial direction of propagation is perpendicular to the channels. In Figure 4.14 the initial propagation is parallel to the channels. In both Figure 4.13 and 4.14 we can see that the channels have a huge impact on the morphology of the dendrites. From the points of nucleation we see traditional branches which continue deep into the samples. However, these main branches have many smaller side branches which follow the direction of the channel pattern in a rather strictly. The length of these smaller branches vary greatly. Even though the branches are very tightly spaced, we can see that they manage to avoid crossing each other. This behavior is also found in traditional dendritical avalanches.

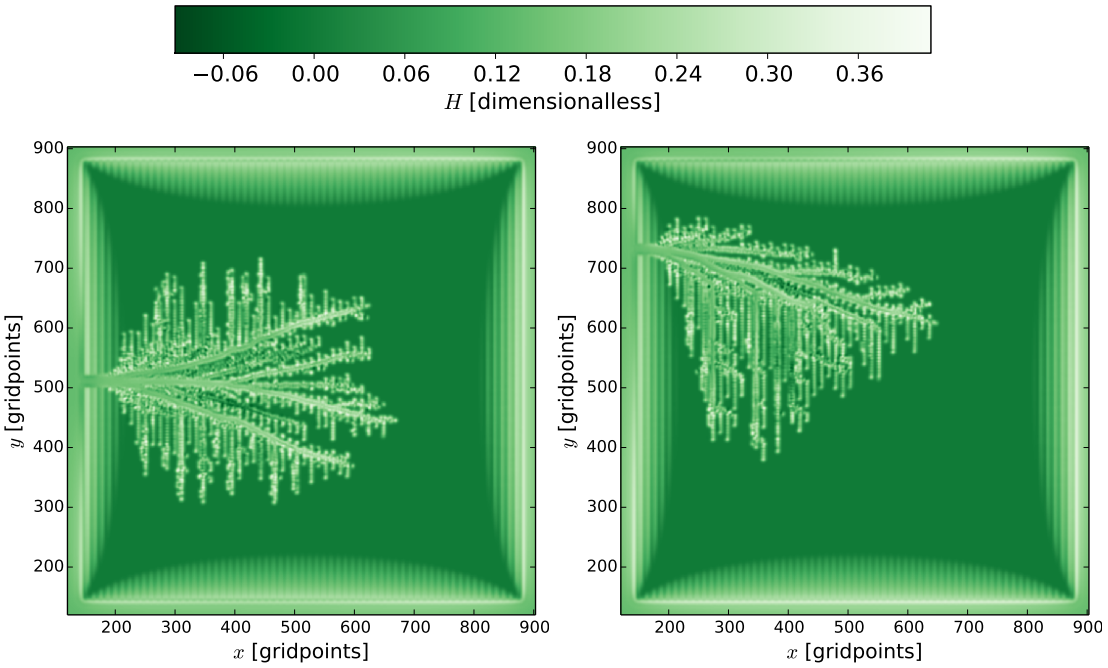

(a) Dendrite triggered on the center of the edge.

(b) Dendrite triggered off center.

Figure 4.13: Simulation results for dendritic avalanches in samples with channels in the vertical direction

We can group the dendrite branches into two groups: primary branches that cross the channels and secondary branches propagate parallel to the channels. Primary branches seem to favor a certain angle relative to the channels and this angle is approximately equal. This angle may have a close relationship to the choice of b, c and J_{c1}/J_{c0}, but this matter will not be investigated in this work. The branches in the uniform samples seem propagate in a range of directions, while the dendrites in samples with channels are restricted to a few general directions.

It is a philosophical question if the latter patterns are dendritic or not. On one hand they contain classical branches, which we have named type primary branches. The secondary branches, on the other hand, have a well defined direction of propagation which are therefore not dendritic at all.

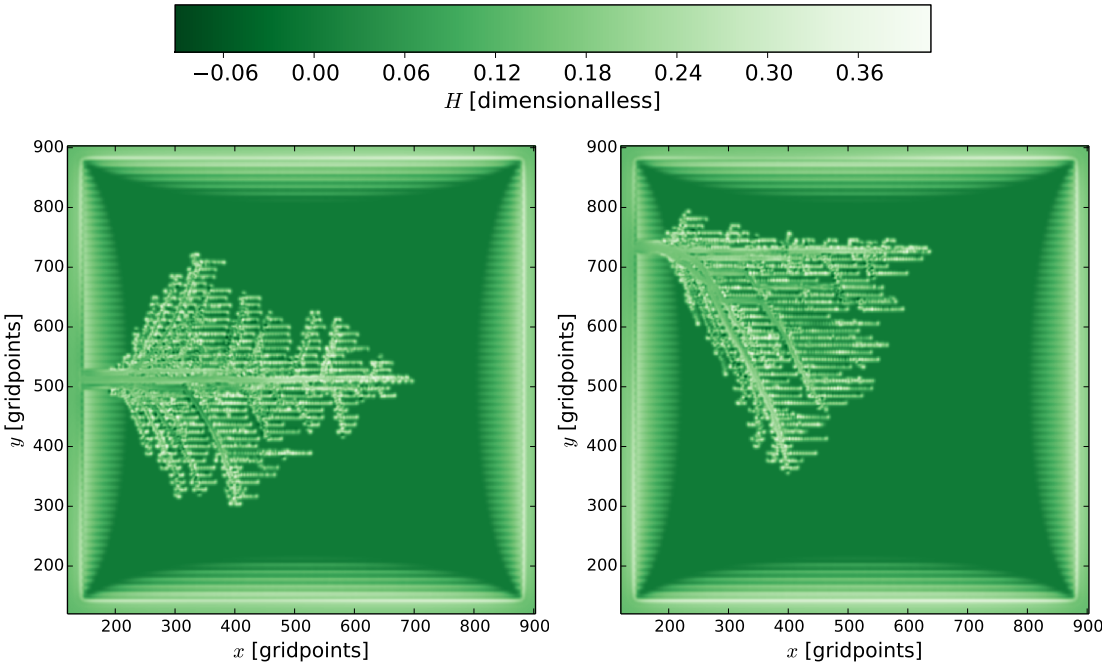

(a) Dendrite triggered symmetrically on the edge.

(b) Dendrite triggered asymmetrically.

Figure 4.14: Simulation results for dendritic avalanches in samples with channels in the horizontal direction.

4.4.1 A closer look at secondary branches

It is natural to assume that the branches of the dendritic avalanches will follow the path of lowest critical sheet current. That is because a lower sheet current density is necessary to destroy the superconducting state in these regions. This section investigates this phenomena in more detail. Thanks to Professor Tom Henning Johansen for suggesting a more detailed study.

In this Section we will start to include information of the underlying matrix of critical sheet current. Then we can do a more thorough analysis of what causes the interesting branching patterns that we have described in the section before.

The simulation program provides us with several types of data that we can visualize. We have already shown images of the magnetic field distribution, the magnitude of current, current streamlines, individual components of the current field and the underlying matrix for the critical sheet current. When we study flux avalanches we should also study also study the temperature field T of the sample as it is central to the feedback loop which destroys the superconducting state.

The information about the critical sheet current will be included by superimposing a transparent layer of the J_c matrix above the image. In practice we scale the J_c matrix by some small value, i.e. 5%, and add this to the matrix we are plotting. As an example we can plot:

$$H(x, y) + 0.05 J_c(x, y),$$

where $H(x, y)$ and J_c are dimensionalless units and J_c varies between 0.75 and 1. In our plots the bright colors correspond to higher values and the dark colors correspond to values closer to zero. Because J_c is lower in the channels, the resulting plots will leave dark lines in the channels and slightly brighter lines where J_c is higher. It is important to note that the additional transparent layer results in an error between the colors in the figure and the actual values. In our plots the colors are about $0.05 - 0.1$ too bright compared to the accompanying colorbars.

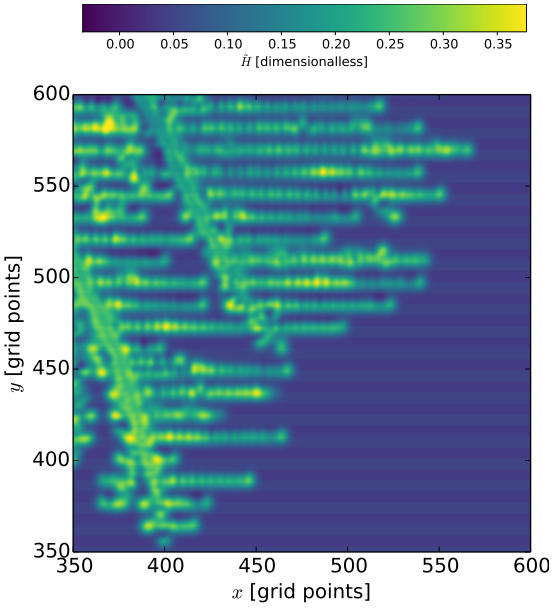

(a) Plot of magnetic field $\tilde{H}(x, y)$

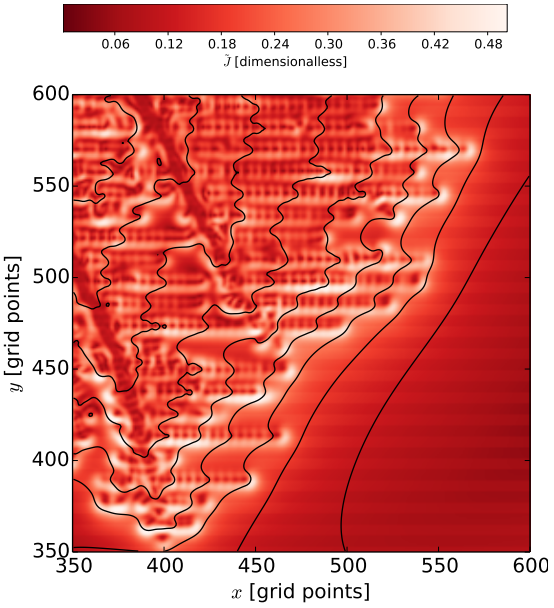

(b) Plot of current $\tilde{J}(x, y)$ and current streamlines.

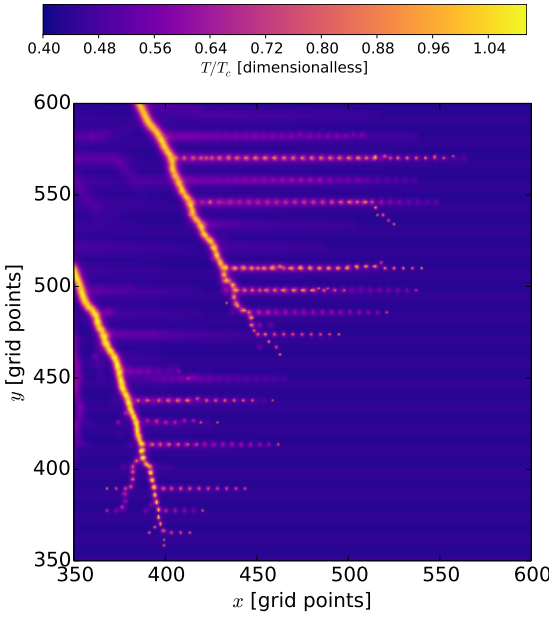

(c) Plot of temperature, $\tilde{T}(x, y)$

Figure 4.15: Closer investigation the flux avalanche in Figure 4.14(b).

In Figure 4.15 we investigate a close up of the avalanche in Figure 4.14(b). Figure 4.15(a) shows the magnetic field (where we welcome a colormap which results in improved contrast) and Figure 4.15(b) shows the magnitude of current, including the current streamlines. Figure 4.15(c) shows the temperature field $\tilde{T}$, where $\tilde{T} = T/T_c$. For these figures we have applied the method of superimposing the J_c matrix.

In Figure 4.15(a) we can see two large primary branches, but the image is dominated by branches following the direction of the channels. Surprisingly the secondary branches are not propagating inside the channels, they are propagating along the boundaries between high and low J_c. Also they do not follow every boundary, only every other boundary. The avalanche in Figure 4.15(a) originates coming from the upper left (outside the boundary of the image), spreading downwards to the right. When the main branches cross a channel, nothing happens until it reaches the other side of the channel where it meets the discontinuous increase in J_c. From here the primary branch splits into a secondary branch. This happens every time the primary branch transitions from low to high J_c and therefore we get a dense pattern of secondary branches with spacing equal to $b + c$. In figure 4.15(a) the primary branches move in the positive x and negative y direction. The secondary branches continue in the positive x direction, which is parallel to the channels. We also see some very small primary avalanches which are moving in the negative x and y direction. Their secondary avalanches continue in the negative x direction. We observe that the secondary avalanches inherit their direction of propagation from the primary branch, but only the component parallel to the channels of course. This phenomenological analysis is consistent with the other simulation results in Figure 4.13 and Figure 4.14.

It is important to note that we are studying phenomena on pixel level and that the critical current density changes discontinuously. These are both factors which decrease the confidence in our analysis.

In Figure 4.15(b) we see that the secondary branches disrupt the current field. Wherever the current streamlines cross the branches, we see kinks in the streamlines with a varying degree of sharpness. We also see that the magnitude of current is at its highest right outside the tips and the side of the branches.

The temperature field in Figure 4.15(c) shows how the temperature is raised inside the dendrite branches. The bright dots we see, where we have secondary branches, are a sign of errors in the numerical calculations. A point of interest is that the primary branches of high temperature are not straight on the tip. Outside the channels we see that the branch moves perpendicular to the channels. Inside the channels the branch bends and becomes more diagonal. When the branch meets the boundary where J_c increases, the channel splits in two: a secondary branch moving parallel to the boundary of the channel and a continuation of the primary avalanche. The latter branch exits the channel perpendicular to the boundary.

4.4.2 Inner avalanches

I made a movie of the evolution of the magnetic field corresponding to Figure 4.14(b) and Jørn Inge Vestgården noticed secondary avalanches inside secondary branches. To show this we provide in Figure 4.16 close up images of the time evolution of H and T/T_c. The J_c field is superimposed on the image with 5% opacity for magnetic field and current, and 10% for temperature. The state of the system was recorded at 50 equidistant time steps during the avalanche in Figure 4.14(b). In this section we study the consecutive time steps from 20-28.

In Figure 4.16 the time steps are sorted so that the upper plots of Figures 4.16(a) and 4.16(b) correspond to the 20th time step and the bottom corresponds to the 28th time step is at the bottom of the figure. In Figure 4.16(a) we see two secondary branches. In the middle of each branch we can see increased intensity which spreads in the positive x-direction. This direction i also the original direction of propagation for these secondary branches. The cause for this reintensification might be that the surrounding branches have stopped propagating and therefore flux must be transferred through existing branches.

The temperature evolution shown in Figure 4.16(b) does not seem to change as dramatically in the secondary branches, but the main branch becomes much warmer. We interpret the individual spots of high temperature as numerical error. In Figure 4.16(b) it is easier to see how the primary branch bends inside the channel and exits the channel perpendicular to the boundary of the channel[2]. The angle between primary branches and the channels are likely related to this bending inside the channels.

[2]The primary branch may not exit the channel perfectly perpendicular to its boundary. However, we are mostly interested in the tendencies in the morphology.

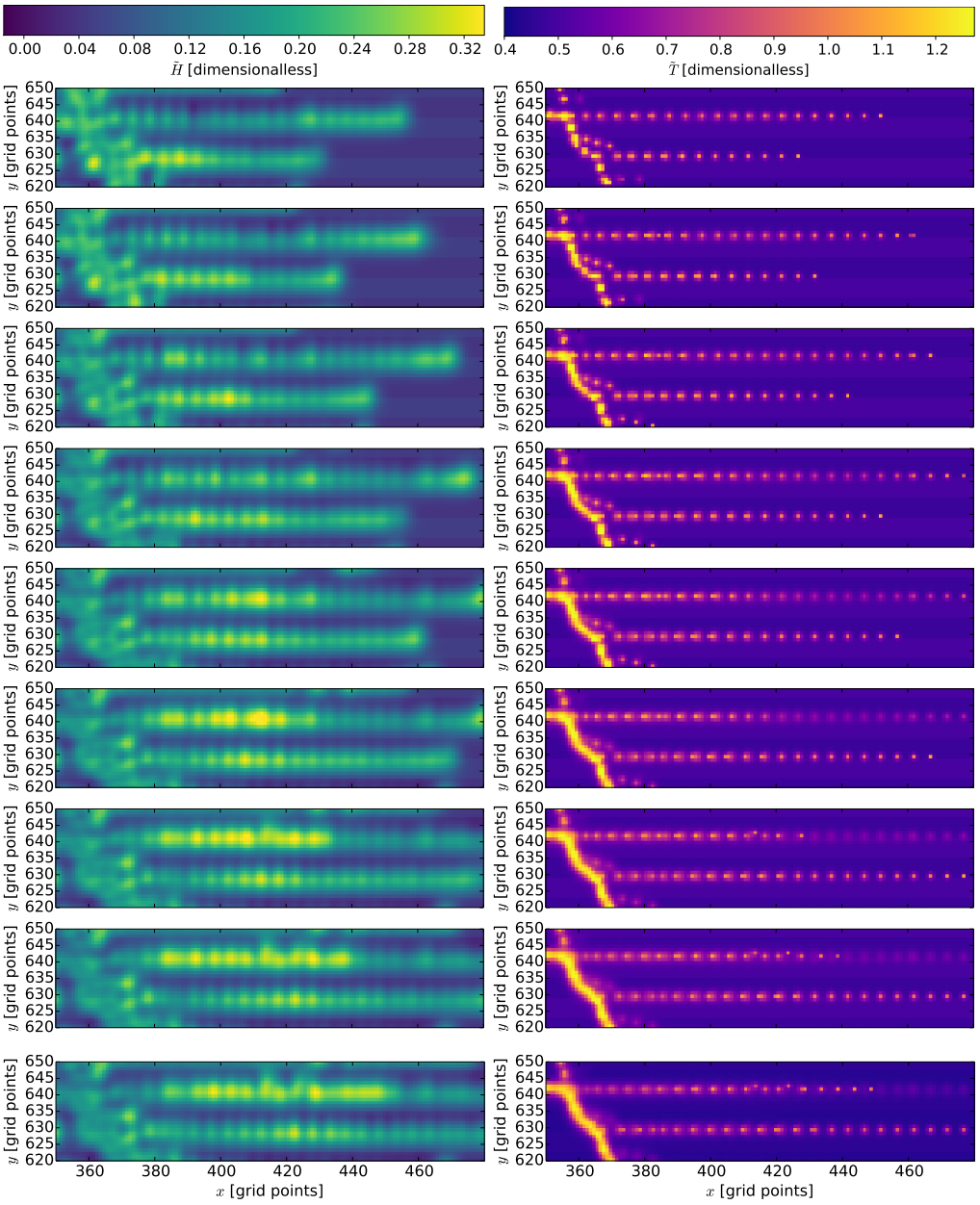

(a) Magnetic field (b) Temperature

Figure 4.16: Inner avalanches observed during propagation of the dendrite in Figure 4.14(b). Each horizontal set of plots correspond to the same time step. The time evolution is ordered from top to bottom and the time intervals between each row of plots are constant.

4.5 Dendrite where one half of the sample has reduced critical current

To get a better understanding of the behavior of secondary branches, we will now study a sample where the northern half of the sample has reduced J_c. Specifically we have chosen $J_{c1}/J_{c2} = 0.5$, which is a very large difference in critical sheet current. The

resolution of the system was 256×256 grid points and the boundary between high and low J_c is between $y = 127$ and $y = 128$. The magnetic field was ramped up to $\tilde{H} = 0.3$ [dimensionalless]. Then a dendrite was triggered off center on the edge so that the dendrite starts in the region where the critical sheet current is lowest. For this section we have not superimposed the underlying J_c data in the plots. In Figure 4.17(a) we can see how the primary branches are deflected and produce secondary branches along the boundary. The dendrites are not able to penetrate into the southern part because the increase in J_c is so much larger in that region. In Figure 4.17(a) we see that the magnitude of the current is low. The highest value is well below $J_{c1}/J_{c0} = 1/2$. We must remember that the critical sheet current is a function of the local temperature. The temperature field is shown in Figure 4.17(c). Whenever

$$T(x, y)/T_c > 1, \tag{4.8}$$

the superconducting state is destroyed at (x, y). The other condition for the superconducting state is that

$$J/J_c < 1. \tag{4.9}$$

In the simulation we have used the following temperature dependence for the critical sheet current:

$$J_c(T) = J_c(1 - T/T_c) \quad \text{for} \quad T < T_c \tag{4.10}$$

Inserting this dependence into Equation 4.9 we get the following two conditions for the superconducting state at (x, y):

$$\begin{gathered} J(x, y)/J_c(x, y)(1 - T/T_c) < 1 \quad \text{for} \quad T < T_c \\ T(x, y)/T_c < 1 \end{gathered} \tag{4.11}$$

If either of the above conditions are not satisfied, we classify the material as normal at (x, y). If both of the conditions are satisfied, we can quantify the local vulnerability $V(x, y, T(x, y))$ of the superconducting state by the ratio $J(x, y)/J_c(x, y, T)$:

$$V(x, y, T) \equiv \frac{J(x, y)}{J_c(x, y, T)} = \frac{J(x, y)}{J_c(x, y)(1 - T/T_c)} \quad \text{for} \quad T < T_c \quad \text{and} \quad J(x, y) < J_c(x, y) \tag{4.12}$$

We define $V(x, y, T) \equiv 1$ whenever $T \geq T_c$ or $J \geq J_c$. From these definitions we can plot $V(x, y)$ as shown in Figure 4.17(d). We see that the vulnerability has a much larger value for $y \geq 128$ than for $y < 128$. $y \geq 128$ corresponds to the part of the sample where J_c has been reduced. All the avalanches propagate in this region and it is obvious that it is more vulnerable to breakdown compared to the other half of the sample.

We will study the largest secondary branch in Figure 4.17 in more detail. In Figure 4.18 we show close up images of the time evolution of $\tilde{H}$ and $J/J_($x, y) for this branch.

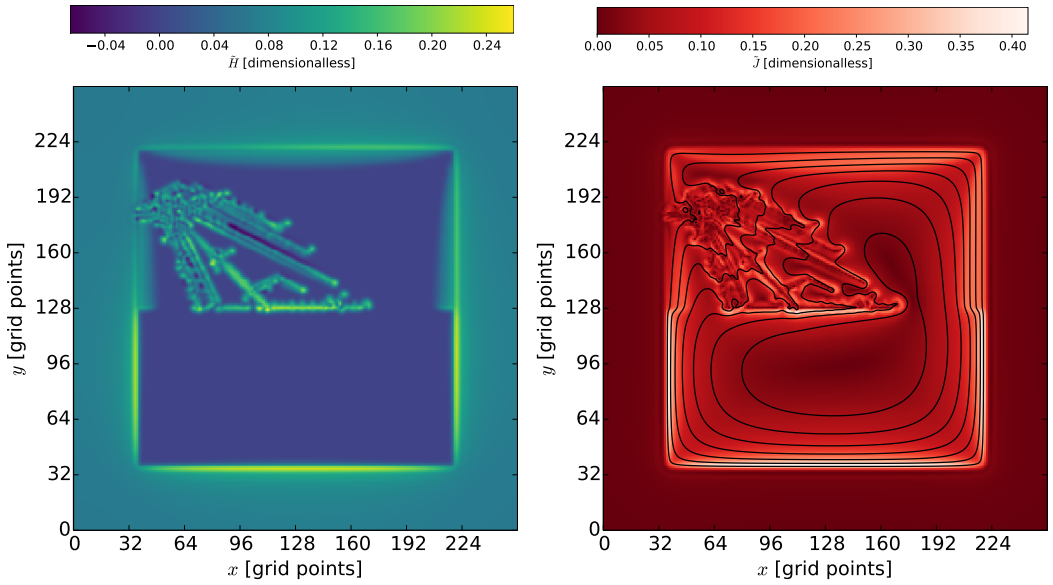

(a) Final state of the magnetic field distribution.

(b) Final state of the current distribution, including current streamlines.

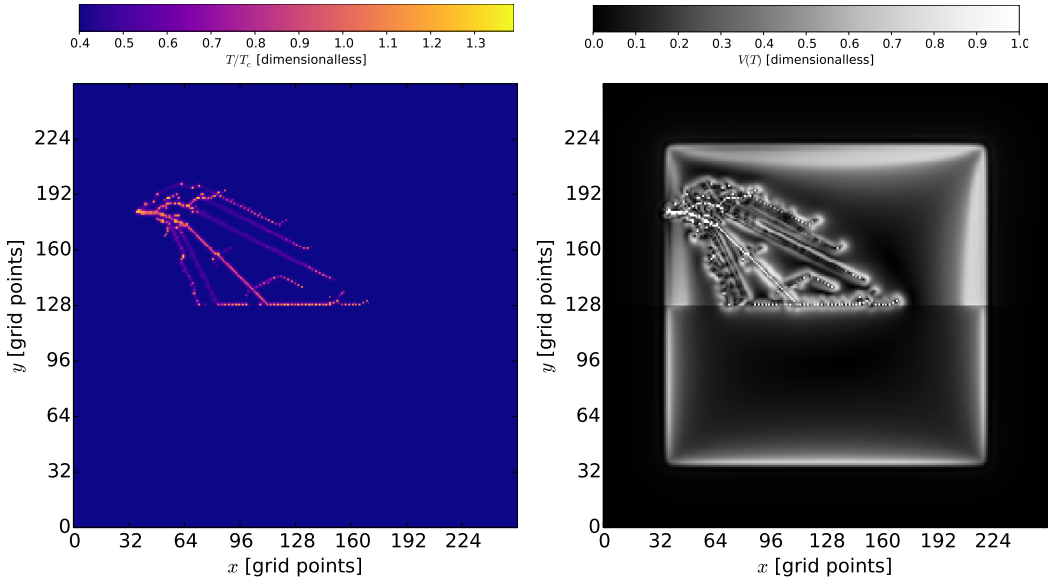

(c) Final state of the temperature field.

(d) The local vulnerability of the superconductor in the final state.

Figure 4.17: The final state of an avalanche in a sample where the northern half has half the critical sheet current relative to the southern part.

Both the magnetic field and the current are the most intense at the point where the primary branch encounters the boundary of the high J_c region. These maxima should be important for the further propagation of primary branches in samples where the avalanche is able to cross the high J_c regions. For this sample the difference in J_c is simply too large for further propagation of the primary branch. In Figure 4.18 we also see a local maxima in field and current at the tip of the secondary branch. The time evolution of the temperature field is shown in Figure 4.19(a). We can see that along

the secondary branch there are many small peaks in temperature(bright dots). This is most likely caused by numerical errors in the simulation, as stated earlier. We see that the temperature traces the boundary very strictly within the time interval that we are studying.

The part of the sample with reduced J_c lies in the region with $y > 127$. This region is much brighter in Figure 4.19(b). Hence its vulnerability is higher. The vulnerability is at its highers at the tip of the secondary branch, at the row $y = 128$ which is the closest row to the region of large J_c. Thus the vulnerability is typically highest at the tip of the secondary branch, close to the boundary between high and low J_c. It is therefore no longer any surprise that the secondary branch follows the boundary, with some exceptions. In this simulation, the primary branch did not propagate into the region of high J_c. If it did, we would expect it to propagate into the pixels (x, y) for which $V(x, y)$ is minimum. In Figure 4.19(b) we see that the pixels at $y = 127$ have a low value. However $V(x, y)$ has a maximum at about $(x = 111, y = 125)$, let us call this point **m**. The primary branch ends at about $(x = 111, y = 128)$, which we can call **e**. If the primary dendrite was to continue propagating along the shortest path from **m** to **e**, it would cross the boundary perpendicularly. This may be the explanation why the primary temperature branch in Figure 4.16(b) tends to cross the channels perpendicularly to the channels. If the difference in J_c is small, we would expect the dendrite to spend minimal time crossing the boundary. In that case it would most likely just cross in the point where it encounters the boundary.

The part of the sample with reduced J_c lies in the region with $y > 127$. This region is much brighter in Figure 4.19(b). Hence its vulnerability is higher. The vulnerability is at its highest at the tip of the secondary branch, at the row $y = 128$ which is the closest row to the region of large J_c. Thus the vulnerability is typically highest at the tip of the secondary branch, close to the boundary between high and low J_c. It is therefore no longer any surprise that the secondary branch follows the boundary, with some exceptions. In this simulation, the primary branch did not propagate into the region of high J_c. If it did, we would expect it to propagate into the pixels (x, y) for which $V(x, y)$ is minimum. In Figure 4.19(b) we see that the pixels at $y = 127$ have a low value. However $V(x, y)$ has a maximum at about $(x = 111, y = 125)$, let us call this point **m**. The primary branch ends at about $(x = 111, y = 128)$, which we can call **e**. If the primary dendrite was to continue propagating from **m** to **e**, it would cross the boundary perpendicularly. This may explanation why the primary temperature branch in Figure 4.16(b) tends to cross the channels perpendicularly to the channels. If the difference in J_c is small, we would expect the dendrite to spend minimal time crossing the boundary. In that case it would most likely cross in the point where it encounters the boundary.

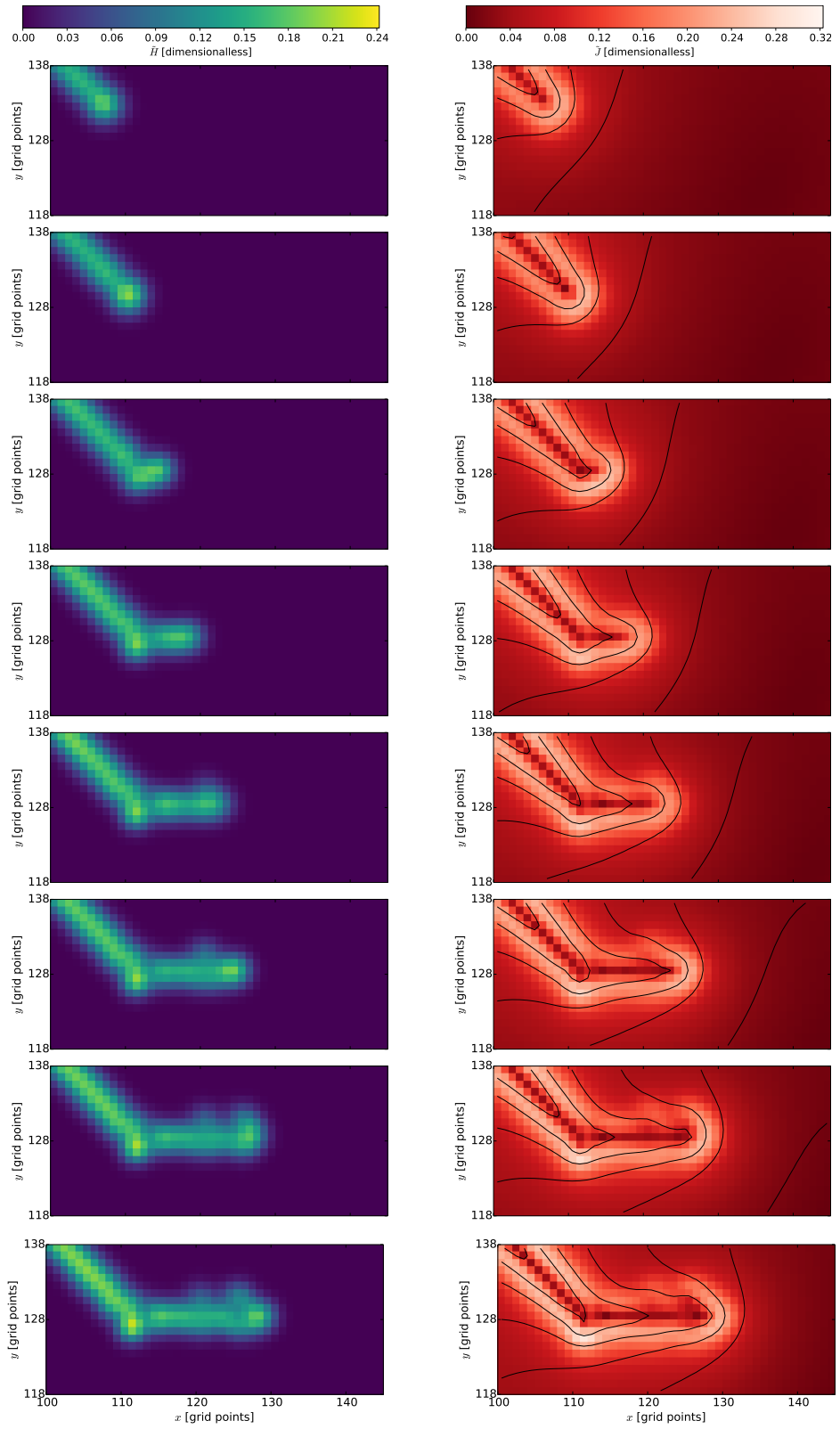

(a) Evolution of the magnetic field around the boundary

(b) Evolution of the current and current streamlines around the boundary

Figure 4.18: Close up time evolution of magnetic field and current at the boundary between high and low J_c.

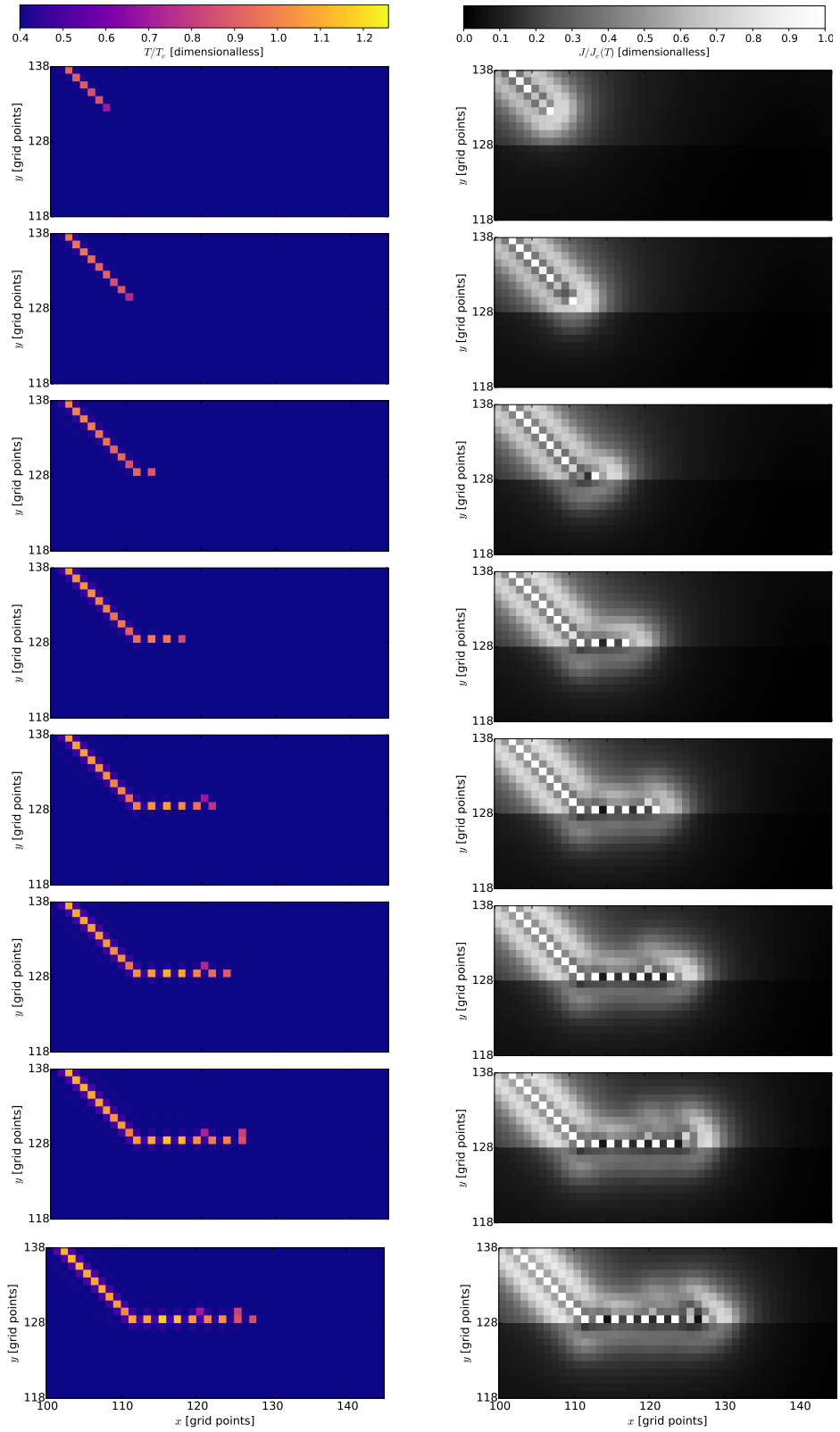

(a) Evolution of temperature around the boundary.

(b) Evolution of vulnerability around the boundary.

Figure 4.19: Close up time evolution of temperature and vulnerability at the boundary between high and low J_c.

Chapter 5

Conclusion

We have invented a method for producing anisotropy in computer simulations of superconducting thin films. This was achieved by reducing the critical sheet current in a stripewise pattern across the film. These stripes of reduced critical sheet current have been called channels and we chose the width of the channels to be equal to the spacing in between them. For samples without flux avalanches, the channels can be interpreted as regions where the thickness of the material is reduced. The current was found to be anisotropic on a length scale much larger than the width of these channels, even though it is isotropic on the microscopic scale.

The resulting anisotropy was much weaker than we expected from our theoretical predictions. It turns out that flux creep destroys the anisotropy we try to produce. If the creep exponent was chosen to be low, i.e. $n = 5$, the anisotropy would vanish. For less flux creep, i.e. $n = 19$, we got a rather weak anisotropic effect. For even higher values of the creep exponent, the simulations were unstable. When our choice of parameters were appropriate, the resulting anisotropy factor was typically measured to be about half of the predicted value.

The largest anisotropy factor $a \approx 1.12$ was found for a sample where the critical sheet current was reduced by 30 % in the channels. However this simulation took more time than for more moderate reductions of J_c. In general the channels introduces numerical instability because of the discontinuous changes in J_c. More gradual variations in J_c will not necessarily resolve this issue. This is because a gradual change is impossible on the length scale of single pixels, even though the discontinuous jumps would be smaller.

An algorithm was developed for the purpose of drawing streamlines in samples with channels. There are some situations where it can be used to assist our intuition about Bean model streamlines. However one must be careful in order to avoid round off errors in the distance between the streamlines.

After the model for anisotropy had been studied we investigated the behavior of magnetic flux avalanches in such samples. The avalanches made dendritic patterns, but

we also observed flux branches which traced the boundaries where J_c increases discontinuously. This type of branches were named *secondary branches*. By studying the local vulnerability of the superconducting state, we found an explanation for this phenomenon. When the avalanche approaches a boundary where J_c increases discontinuously, the boundary was found to be vulnerable to breakdown.

Inside secondary branches we found secondary avalanches. This is seen as reintensification of the magnetic flux inside the branch.

From our research we have increased our understanding of magnetic flux avalanches in samples where the critical current density is not uniform. If nontraditional branching patterns are observed in experiments, one should consider the possibility that perturbations in J_c may be the explanation. However in real samples we would expect the variation of J_c to be more subtle and thus the secondary branches would also be more subtle.

There are still matters that should be investigated when it comes to avalanches in samples with channels. Obviously we would like to see experimental verification. However it will be difficult to synthesize this type of samples. In our simulations we would like to investigate branching patterns in samples where the perturbations are more subtle.

Appendix A

Program code for simulating streamlines in a sample assuming a Bean model

Main program written in the Julia programming language[1]:

```
include("helpingfunctions.jl")
outfile = "streamlines.csv"
infilename = "jc.csv"
numberOfLines = 50

data =  initialize(infilename, numberOfLines)

J = solve(data)
println("I am done with computing the streamlines,
but I have to write the data to file.")

writecsv(outfile, float(J))
print("I am done with everything. Data stored in "
 * string(outfile) )
```

File "helpingfunctions.jl":

```
function initialize(filename, numberOfLines::Int64)

    # critical current init:
    jc = readcsv("jc.csv")
    s = size(jc)

    #rows and collumns:
    nx = s[1]
    ny = s[2]

    # distance between streamlines:
    distance = zeros(Int64, (nx,ny))
    distanceScaling = round(min(nx, ny) / (2.0*numberOfLines))
```

[1]See http://julialang.org/ for the official documentation of the Julia programming language.

```
    println("nx, ny = " * string(nx) * ", " *string(ny))
    println("distanceScaling = " * string(distanceScaling))
    for i in 1:nx
        for j in 1:ny
            distance[i,j] = round(distanceScaling/jc[i,j])
        end
    end

    # The matrix of current stream lines:
    J = falses(nx, ny)
    J[1,:] = true
    J[nx,:] = true
    J[:,ny] = true
    J[:,1] = true

    # the indices for which J[currIndX[k],currIndY[k]]
    # are true:
    currIndX = Int64[]
    currIndY = Int64[]

    for i in 1:nx
        for j in 1:ny
            if J[i,j]
                push!(currIndX, i)
                push!(currIndY, j)
            end
        end
    end

    # boolean matrix init:
    boolMat = trues(nx,ny)

    return (distance, J, nx, ny, currIndX, currIndY, boolMat)

end


function solve(data)
    dist, J, nx, ny, currIndX, currIndY, boolMat= data

    # As long as there is space for more current in the current
    # matrix J:
    while any1(boolMat)
        # Update which elements of the sample that we are allowed
        # to add current to:
        updateBoolMat(currIndX, currIndY, dist, nx, ny, boolMat)
        # From a new boolean matrix created above we will
        # drawCurrentline the next iteration of current lines:
        currIndX, currIndY = drawCurrentline(boolMat, J, nx, ny)
    end

    return J
end

"""
```

```
Checks if multidimensional bitarray has a 1
returns true if one or more elements contains 1
"""
function any1(mat::BitArray{2})
    s = size(mat)
    for h in 1:s[1]
        for k in 1:s[2]
            if mat[h,k]
                return true
            end
        end
    end
    return false
end

"""
Given the indices of the latest streamlines,
the function modifies the booleanMatrix.
The elements of the booleanMatrix which are
within a certain distance of streamline elements
are set to zero.
"""
function updateBoolMat(currIndX::Array{Int64,1},
                       currIndY::Array{Int64,1},
                       distance::Array{Int64,2},
                       nx::Int64, ny::Int64,
                       bolsk_matrise::BitArray{2})

    s = size(currIndX)
    length = s[1]

    # Iterate through the elements that are within
    # a distance distance[x,y] of element (x,y)
    for k in 1:length
        x = currIndX[k]
        y = currIndY[k]

        spacing = distance[x,y]
        spacing2 = spacing*spacing
        i_min = max(x - spacing, 1)
        i_max = min(x + spacing, nx)

        for i in i_min:i_max
            deltaX = i-x
            deltaX2 = deltaX*deltaX
            inted_semi_circle = isqrt(spacing2 - deltaX2)

            j_min = max(1,  y - inted_semi_circle )
            j_max = min(ny, y + inted_semi_circle)
            for j in j_min:j_max
                bolsk_matrise[i,j] = 0
            end
        end
    end
end
```

```
function testIfNeighboursHave0(mat::BitArray{2},
                               x::Int64, y::Int64,
                               nx::Int64, ny::Int64)
    # Avoid index out of bouds errors:
    i_min = max(1,x-1)
    j_min = max(1,y-1)
    i_max = min(nx,x+1)
    j_max = min(ny,y+1)

    # check elements:
    for i in i_min:i_max
        for j in j_min:j_max
            if !mat[i,j]
                return true
            end
        end
    end

    # returns false if no zeros in neighbours
    return false
end

"""
Given a BitArray{2}, yields an the indices of
where current lines should be placed.
"""
function drawCurrentline(boolMat::BitArray{2},
                         J::BitArray{2}, nx::Int64,
                         ny::Int64)
    currIndX = Int64[]
    currIndY = Int64[]

    for i in 1:nx
        for j in 1:ny
            # if the element is true and at least one of its
            # neighbours are false
            if boolMat[i,j] && testIfNeighboursHave0(boolMat,
                                                     i, j,
                                                     nx, ny)
                # Dra a pixel of current
                J[i,j] = 1
                # Add the indices of new current pixel to the
                # current indices:
                currIndX = push!(currIndX, i)
                currIndY = push!(currIndY, j)
            end
        end
    end

    return currIndX , currIndY
end
```

Appendix B

Program code for calculating magnetic field from segments of current

Main program:

```
include("helpingfunctions.jl")

filenameForJx = "jx.csv"
outfilename = "resultatH.csv"
JcInfilename = "jc.csv"
startIndex = 146

# We have to make a matrix for the current:
jx, nx, ny = makeJx(JcInfilename, 1.0958,-13.988, startIndex, filenameForJx)

# Then calculate the magnetic field from the current matrix:
magneticField = zeros(nx,ny)
magneticField = startCalculations(magneticField, jx, nx, ny)

# Write results to file:
writecsv(outfilename, magneticField)
println("Done with calculations")
```

File "helpingfunctions.jl":

```
"""
Starts and runs the calculation of the magnetic field.
"""
function startCalculations(magneticField::Array{Float64,2},
                           jx::Array{Float64,2}, nx::Int64, ny::Int64)

  half = round(Int64, nx/2)
  for i in 1:nx
    for j in 1:ny
      if abs(jx[i,j]) > 0.0
        H(i, j, magneticField, jx[i,j], nx, ny)
      end
```

```
    end
    println(i)
  end
  magneticField = magneticField / (4.0*pi)
  return magneticField
end

"""
For the special case of current parallel to the x direction,
the function H calculates the z component of the magnetic field,
contributed by the current in current[x,y], in the x,y plane
"""
function H(x::Int64, y::Int64, field::Array{Float64, 2},
                  current::Float64, nx::Int64, ny::Int64)
  for i in 1:nx
    cathetus_x = i-x
    # Precalculate some reused variables:
    cathetus_x2= float(cathetus_x * cathetus_x)
    current_cathetus_x= current * cathetus_x
    # If i = x => dB[i,:] = 0, i != x => (x,y) != (i,j)
    if (i!=x)
      for j in 1:ny
        cathetus_y= float(j-y)
        hypotenuse = sqrt(cathetus_x2 + cathetus_y*cathetus_y)
              field[i,j] += current_cathetus_x /hypotenuse^3
      end
    end
  end
end

"""
Only works for jc.txt with two different values
"""
function makeJx(filenameJc, gradient::Float64,
        constant::Float64, start::Int64, outFilenameJx)

  jc = readcsv(filenameJc)
  nx, ny = size(jc)
  jx = zeros(nx, ny)

  Jmax = float(maximum(jc))
  Jmin = float(minimum(jc))
  averageJc = (Jmax+Jmin)/2.0

  i = start
  ymin = round(Int, gradient*i + constant)
  ymax = round(Int, ny/2)

  # We need to set the currents in a triangle:
  while ymin < ymax
    ymax = ny/2
    for j in ymin:ymax
      # If jc is not the high value
      if abs(jc[j,i]) < averageJc
        jx[i,j]=Jmin
```

```
      else
        jx[i,j]=Jmax
      end
    end
    i+=1
    ymin = round(Int, gradient*i + constant)
  end

  writecsv(outFilenameJx, jx)
  return jx, nx, ny
end
```

Bibliography

[1] P Müller and A.V.Ustinov. *The physics of superconductors*. Springer, 1997. ISBN 9783540612438.

[2] W. Meissner and R. Ochsenfeld. Ein neuer effekt bei eintritt der supraleitfähigkeit. *Naturwissenschaften*, 21(44):787–788, 1933. ISSN 1432-1904. doi: 10.1007/BF01504252. URL http://dx.doi.org/10.1007/BF01504252.

[3] F. London and H. London. The electromagnetic equations of the supraconductor. *Proceedings of the Royal Society of London A: Mathematical, Physical and Engineering Sciences*, 149(866):71–88, 1935. ISSN 0080-4630. doi: 10.1098/rspa.1935.0048. URL http://rspa.royalsocietypublishing.org/content/149/866/71.

[4] L Landau. On the theory of phase transitions. *Collected Papers, Nauka, Moscow*, Vol. 1:234–252, 1969. URL http://www.ujp.bitp.kiev.ua/files/journals/53/si/53SI08p.pdf. Originally published in Zh. Eksp. Teor. Fiz. 7, pp. 19-32 (1937).

[5] A. A. Abrikosov. On the magnetic properties of superconductors of the second group. *Soviet Physics JETP*, 5, June 1957. URL http://www.mn.uio.no/fysikk/english/research/groups/amks/superconductivity/vortex/1957.html.

[6] U. Essmann and H. Träuble. The direct observation of individual flux lines in type ii superconductors. *Physics Letters A*, 24(10):526 – 527, 1967. ISSN 0375-9601. doi: http://dx.doi.org/10.1016/0375-9601(67)90819-5. URL http://www.sciencedirect.com/science/article/pii/0375960167908195.

[7] Nobel Prize website. Type ii superconductors and the vortex lattice, 2003. URL https://www.nobelprize.org/nobel_prizes/physics/laureates/2003/abrikosov-facts.html.

[8] Ernst Helmut Brandt. Electric field in superconductors with rectangular cross section. *Phys. Rev. B*, 52:15442–15457, Dec 1995. doi: 10.1103/PhysRevB.52.15442. URL http://link.aps.org/doi/10.1103/PhysRevB.52.15442.

[9] P. W. ANDERSON and Y. B. KIM. Hard superconductivity: Theory of the motion of abrikosov flux lines. *Rev. Mod. Phys.*, 36:39–43, Jan 1964. doi: 10.1103/RevModPhys.36.39. URL http://link.aps.org/doi/10.1103/RevModPhys.36.39.

[10] Y. B. Kim, C. F. Hempstead, and A. R. Strnad. Critical persistent currents in hard superconductors. *Phys. Rev. Lett.*, 9:306–309, Oct 1962. doi: 10.1103/PhysRevLett.9.306. URL http://link.aps.org/doi/10.1103/PhysRevLett.9.306.

[11] P. W. Anderson. Theory of flux creep in hard superconductors. *Phys. Rev. Lett.*, 9:309–311, Oct 1962. doi: 10.1103/PhysRevLett.9.309. URL http://link.aps.org/doi/10.1103/PhysRevLett.9.309.

[12] C. P. Bean. Magnetization of hard superconductors. *Phys. Rev. Lett.*, 8:250–253, Mar 1962. doi: 10.1103/PhysRevLett.8.250. URL http://link.aps.org/doi/10.1103/PhysRevLett.8.250.

[13] E. Zeldov, John R. Clem, M. McElfresh, and M. Darwin. Magnetization and transport currents in thin superconducting films. *Phys. Rev. B*, 49:9802–9822, Apr 1994. doi: 10.1103/PhysRevB.49.9802. URL http://link.aps.org/doi/10.1103/PhysRevB.49.9802.

[14] Bruker's web-site, 04 2016. URL https://www.bruker.com/products/superconductors-and-metal-composite-materials/superconductors/ybco-2g-hts-superconductors/overview.html. Retrieved on 27th of April 2016.

[15] R. C. Black, A. Mathai, F. C. Wellstood, E. Dantsker, A. H. Miklich, D. T. Nemeth, J. J. Kingston, and J. Clarke. Magnetic microscopy using a liquid nitrogen cooled yba2cu3o7 superconducting quantum interference device. *Applied Physics Letters*, 62(17):2128–2130, 1993. doi: http://dx.doi.org/10.1063/1.109448. URL http://scitation.aip.org/content/aip/journal/apl/62/17/10.1063/1.109448.

[16] J I Vestgården, P Mikheenko, Y M Galperin, and T H Johansen. Nonlocal electrodynamics of normal and superconducting films. *New Journal of Physics*, 15(9):093001, 2013. URL http://stacks.iop.org/1367-2630/15/i=9/a=093001.

[17] P. Esquinazi, R. Höhne, Y. Kopelevich, A. V. Pan, and Ziese. Mechanical and squid measurements on nb thin films: Learning from a conventional superconductor. *NATO ASI series. Series E, Applied sciences*, 356:149–172, 1999.

[18] V.K. Vlasko-Vlason et al. Magneto-optical studies of magnetization processes in high-tc superconductorsstructure. *NATO ASI series. Series E, Applied sciences*,

356:205–237, 1999. URL http://www.osti.gov/scitech/servlets/purl/11169.

[19] T. H. Johansen, M. Baziljevich, D. V. Shantsev, P. E. Goa, Y. M. Gal pe rin, W. N. Kang, H. J. Kim, E. M. Choi, M.-S. Kim, and S. I. Lee. Dendritic magnetic instability in superconducting mgb 2 films. *EPL (Europhysics Letters)*, 59(4):599, 2002. URL http://stacks.iop.org/0295-5075/59/i=4/a=599.

[20] C. A. Durán, P. L. Gammel, R. E. Miller, and D. J. Bishop. Observation of magnetic-field penetration via dendritic growth in superconducting niobium films. *Phys. Rev. B*, 52:75–78, Jul 1995. doi: 10.1103/PhysRevB.52.75. URL http://link.aps.org/doi/10.1103/PhysRevB.52.75.

[21] D. V. Denisov, D. V. Shantsev, Y. M. Galperin, Eun-Mi Choi, Hyun-Sook Lee, Sung-Ik Lee, A. V. Bobyl, P. E. Goa, A. A. F. Olsen, and T. H. Johansen. Onset of dendritic flux avalanches in superconducting films. *Phys. Rev. Lett.*, 97:077002, Aug 2006. doi: 10.1103/PhysRevLett.97.077002. URL http://link.aps.org/doi/10.1103/PhysRevLett.97.077002.

[22] F. Colauto, E. Choi, J. Y. Lee, S. I. Lee, E. J. Patiño, M. G. Blamire, T. H. Johansen, and W. A. Ortiz. Suppression of flux avalanches in superconducting films by electromagnetic braking. *Applied Physics Letters*, 96(9):092512, 2010. doi: http://dx.doi.org/10.1063/1.3350681. URL http://scitation.aip.org/content/aip/journal/apl/96/9/10.1063/1.3350681.

[23] M Baziljevich, A.V Bobyl, D.V Shantsev, E Altshuler, T.H Johansen, and S.I Lee. Origin of dendritic flux patterns in mgb2 films. *Physica C: Superconductivity*, 369:1-4:93 – 96, 2002. ISSN 0921-4534. doi: http://dx.doi.org/10.1016/S0921-4534(01)01226-6. URL http://www.sciencedirect.com/science/article/pii/S0921453401012266.

[24] Eun-Mi Choi, V V Yurchenko, T H Johansen, Hyun-Sook Lee, Jae Yeap Lee, Won Nam Kang, and Sung-Ik Lee. Suppression of dendritic flux jumps in mgb 2 films coated with a gold rim. *Superconductor Science and Technology*, 22(1):015011, 2009. URL http://stacks.iop.org/0953-2048/22/i=1/a=015011.

[25] T H Johansen, M Baziljevich, D V Shantsev, P E Goa, Y M Galperin, W N Kang, H J Kim, E M Choi, M-S Kim, and S I Lee. Dendritic flux patterns in mgb2 films. *Superconductor Science and Technology*, 14(9):726, 2001. URL http://stacks.iop.org/0953-2048/14/i=9/a=319.

[26] U. Bolz, B. Biehler, D. Schmidt, B.-U. Runge, and P. Leiderer. Dynamics of the dendritic flux instability in $YBa_2Cu_3O_{7-\delta}$ films. *Europhys. Lett.*, 64(4), 2003.

[27] J. Albrecht, A. T. Matveev, J. Strempfer, H.-U. Habermeier, D. V. Shantsev, Y. M. Galperin, and T. H. Johansen. Dramatic role of critical current anisotropy on flux avalanches in mgb_2 films. *Phys. Rev. Lett.*, 98:117001, Mar 2007. doi: 10.1103/PhysRevLett.98.117001. URL http://link.aps.org/doi/10.1103/PhysRevLett.98.117001.